

1 **Novel insights into deep groundwater exploration by geophysical estimation of**
2 **hard rock permeability**

3 **Muhammad Hasan** ^{1, 2, 3,*}, **Lijun Su** ^{1, 2, 3, **}

4 ¹ *State Key Laboratory of Mountain Hazards and Engineering Resilience, Institute of Mountain*
5 *Hazards and Environment, Chinese Academy of Sciences, Chengdu 610299, China*

6 ² *China-Pakistan Joint Research Center on Earth Sciences, CAS-HEC, Islamabad, Pakistan*

7 ³ *University of Chinese Academy of Sciences, Beijing 100049, China*

8

9 *Corresponding authors:

10 Muhammad Hasan: Email: mhasan@imde.ac.cn; ORCID: [https://orcid.org/0000-0001-6804-](https://orcid.org/0000-0001-6804-7962)
11 [7962](https://orcid.org/0000-0001-6804-7962); Phone Number: +86-13051361710

12 Lijun Su: Email: sulijun1976@163.com; ORCID: <https://orcid.org/0000-0001-9972-4698>

13 Corresponding authors' postal address: State Key Laboratory of Mountain Hazards and
14 Engineering Resilience, Institute of Mountain Hazards and Environment, Chinese Academy of
15 Sciences, Chengdu 610299, China

16

17

18

19

20

21

22

23 **Abstract**

24 Deep groundwater exploration in hard rock terrains is critical in regions where deep aquifers may
25 offer long-term water security amidst an increasing scarcity. However, such exploration is
26 globally challenged by geological complexity and the limitations of traditional investigative
27 techniques. Accurate estimation of hydraulic parameters, particularly permeability (k), is
28 essential for effective groundwater management and future resource planning. Conventional
29 borehole-based methods for measuring k are invasive, costly, time-consuming, and **limited to**
30 **sparse, point-scale observations**, making them inadequate for characterizing deep and
31 heterogeneous aquifer systems. Geophysical methods offer a promising non-invasive alternative,
32 enabling broader spatial coverage with reduced surface disturbance. Previous empirical
33 geophysical approaches, such as vertical electrical sounding (VES), are generally restricted to
34 shallow depths (<200 m), relatively homogeneous geological settings, and one-dimensional
35 interpretations. This study demonstrates, for the first time, the use of controlled-source audio-
36 frequency magnetotellurics (CSAMT) to estimate two- and three-dimensional k distributions to
37 depths exceeding 1 km in crystalline and sedimentary terrains. The method relies on an empirical
38 resistivity–permeability relationship calibrated using 116 core samples from six boreholes (0–
39 200 m). While the specific equation derived in this study is site-specific to the Jinji area and
40 should not be directly transferred elsewhere, the broader methodology, integrating CSAMT
41 resistivity with local borehole calibration, offers a transferable framework for k estimation in
42 other complex geological settings. The results show that CSAMT, when calibrated with borehole
43 data, can reliably capture deep subsurface variability and produce spatially continuous
44 hydrogeological models in hard rock terrains. While CSAMT inversion is inherently ill-posed,
45 the incorporation of ground-truth data significantly enhances model robustness and

Formatted: Font: (Default) Times New Roman, 12 pt

Formatted: Font: (Default) Times New Roman, 12 pt

Formatted: Font: Italic

Formatted: Font: (Default) Times New Roman, 12 pt

46 interpretability. By reducing dependence on extensive drilling, this approach represents a
47 significant advancement in deep groundwater exploration. It provides a scalable methodology for
48 sustainable groundwater resource management, while emphasizing the need for local calibration
49 in any new application.

Formatted: Font: (Default) Times New Roman, 12 pt

50 **Keywords:** Permeability; Geophysical methods; Hydraulic parameters; Groundwater; Hard rock;
51 Hydrogeological models

52 **1 Introduction**

Formatted: Space Before: 1 line, After: 1 line

53 Metamorphic and igneous rocks dominate Earth's crust and cover about one-third of its surface
54 (Amiotte Suchet et al., 2003). In hard rock terrains, groundwater research focuses on delineating
55 subsurface structures, such as faults and fractures that control water storage and flow (Fernando
56 and Pacheco, 2015; Hasan et al., 2021). A key parameter in this context is aquifer potential,
57 which reflects the capacity of rock formations to store and transmit groundwater and is
58 influenced by lithology, structural complexity, mineral composition, weathering, and infiltration
59 depth (Majumdar and Das, 2011; Zhu et al., 2017). However, accurately characterizing the
60 lateral and vertical heterogeneity of these properties remains challenging due to limited data and
61 the complexity of massive rock units (Dewandel et al., 2006). In such settings, conventional
62 methods often fall short, leading to inefficient or unsustainable groundwater development
63 (Nwosu et al., 2013; Worthington et al., 2016). Developing cost-effective and reliable
64 approaches for subsurface assessment is therefore essential for managing groundwater in hard
65 rock environments.

66 Groundwater at depths beyond 500 m is typically isolated from surface hydrological
67 influences and often exhibits brackish or saline characteristics (Ferguson et al., 2023). Its

68 strategic importance is increasingly recognized, particularly in geologically- and
69 environmentally-constrained settings (Gleeson et al., 2014). In the Jinji region, several factors
70 necessitate focused investigation of deep aquifers. Surface water is scarce and unreliable, while
71 the shallow subsurface is dominated by fresh granite, which has inherently low porosity and
72 permeability, limiting groundwater availability. By contrast, deeper fractured zones in granite,
73 sandstone, and hornstone present more favorable hydrogeological conditions. Recent national
74 water initiatives in China have emphasized deep subsurface exploration in structurally complex
75 terrains to identify underutilized aquifers for enhancing long-term water security.
76 Comprehensive assessment of these deep reserves is essential to evaluate their recharge potential
77 and integrate them into sustainable resource management strategies (Condon et al., 2020; Hasan
78 and Shang, 2022). As pressure on surface and shallow groundwater intensifies, deep aquifers
79 may serve as a vital buffer against increasing environmental and socio-economic stress.

80 Multiple studies have documented the rapid depletion of global groundwater reserves,
81 raising serious concerns about long-term water sustainability (Wada et al., 2010; Laghari et al.,
82 2012; Jasechko et al., 2024). Addressing this challenge requires accurate and detailed
83 assessments of groundwater resources, which depend critically on a clear understanding of
84 subsurface hydraulic properties. Permeability (k) is a key parameter that describes the ease with
85 which fluids can move through a porous medium, while the capacity to store water is more
86 directly characterized by porosity. This parameter is crucial for aquifer analysis in various
87 hydrogeological settings (Allègre et al., 2016; Esmailpour et al., 2023; Carbillet et al., 2024).
88 Borehole testing remains the standard method for estimating k and related aquifer parameters
89 (De Lima and Niwas, 2000; Hasan et al., 2021). However, borehole investigations are often
90 limited by high costs, logistical challenges, and poor spatial coverage, particularly in rugged

91 terrains, while offering only localized information with limited ability to image lateral and deep
92 structures (Singh, 2005; Fiandaca et al., 2018). These limitations contribute to uncertainties in
93 groundwater assessments, especially in data-scarce regions (Hasan and Shang, 2022).
94 Alternatively, it is essential to develop methods that minimize reliance on costly drilling while
95 still enabling reliable estimation of permeability within prospective rock formations.

96 Geophysical methods are widely and effectively employed to enhance subsurface
97 characterization in groundwater studies (Daily et al., 1992; Jardani et al., 2007; Hinnell et al.,
98 2010; Fu et al., 2013; Jiang et al., 2014; Kouadio et al., 2023). Compared to conventional
99 drilling, these techniques offer significant advantages in cost, deployment speed, environmental
100 impact, and spatial extent (Hu et al., 2013; Fusheng et al., 2022). Their ability to image ~~both~~
101 ~~vertical and lateral~~ subsurface variations in both vertical and lateral dimensions makes them
102 particularly effective in heterogeneous terrains (Hasan et al., 2025). Among them, resistivity-
103 based methods are widely used due to their sensitivity to lithology, porosity, fractures, and fluid
104 content (Hasan et al., 2021; Asfahani, 2023). Common techniques include electrical resistivity
105 tomography (ERT), vertical electrical sounding (VES), and electromagnetic methods such as
106 magnetotellurics (MT), time-domain electromagnetics (TDEM), and controlled-source audio-
107 frequency magnetotellurics (CSAMT) (Soupios et al., 2007; Bauer-Gottwein et al., 2010;
108 Pollock and Cirpka, 2012; Jiang et al., 2014; Di et al., 2020). A comparative summary of these
109 methods (Table 1) highlights their relative strengths and limitations in terms of depth
110 penetration, spatial resolution, sensitivity to cultural noise, and cost. VES is cost-effective but
111 limited to shallow one-dimensional profiling (<200 m) (Niwas and De Lima, 2003; Majumdar
112 and Das, 2011). ERT improves resolution and enables 2D/3D imaging up to ~300 m but requires
113 intensive fieldwork and is less effective in extreme resistivity environments (Abbas et al., 2022;

114 Hasan and Shang, 2022). For deeper targets, electromagnetic methods such as TDEM, MT, and
115 CSAMT are often employed (Bauer-Gottwein et al., 2010; Di et al., 2020; Gonzalez-Duque et
116 al., 2024). MT achieves the greatest depth penetration (up to tens of kilometers) but often
117 sacrifices resolution in the upper crust and is highly susceptible to cultural noise (Simpson and
118 Bahr, 2005). TDEM provides rapid deployment and intermediate depth coverage (hundreds of
119 meters) but suffers reduced sensitivity in resistive hard rock (Bauer-Gottwein et al., 2010). By
120 contrast, CSAMT bridges these approaches: with a controlled source and frequency tuning, it
121 achieves intermediate-to-deep penetration (>1000 m) with improved resolution in resistive hard
122 rock settings and strong immunity to cultural noise (Smith and Booker, 1991; Zonge and
123 Hughes, 1991; Wang et al., 2015; Zhang et al., 2021). The choice between resistivity and
124 electromagnetic techniques is contingent upon parameters like investigation depth, resolution
125 requirements, geological complexity, and logistical constraints (Majumdar and Das, 2011; Hasan
126 et al., 2025). Given the objectives of this study, to characterize deep fractured aquifers in
127 crystalline and sedimentary rocks under complex geological conditions, CSAMT was selected as
128 the most suitable technique. Its combination of depth penetration, resolution, and robustness
129 against noise provides a practical balance between regional coverage and site-specific imaging,
130 enabling the development of 2D and 3D permeability models that are otherwise difficult to
131 achieve with alternative methods.

132 In fractured rocks like granite, metamorphic, and sandstone formations, fluid flow is
133 largely controlled by fracture networks rather than matrix porosity. Accurate hydraulic
134 assessment in such settings benefits from integrated geophysical and hydrogeological approaches
135 to better capture spatial variability and improve flow modeling (Hasan et al., 2021; Abbas et al.,
136 2022). Resistivity-based techniques are particularly valuable for delineating subsurface structures

137 and identifying water-bearing zones. Because electrical resistivity is sensitive to porosity,
138 saturation, fracture density, and fluid salinity, it is increasingly used to infer k in heterogeneous
139 geological settings (Mudunuru et al., 2022; Yan et al., 2024). Permeability is influenced by
140 numerous parameters, including porosity, fracture density and orientation, grain size distribution,
141 degree of weathering, pore connectivity, and saturation level, highlighting the utility of
142 resistivity measurements as indicators for evaluating groundwater flow potential (Gerke et al.,
143 2011; Worthington et al., 2016; Pellet et al., 2024).

144 Empirical and semi-empirical models have been developed to estimate hydraulic
145 properties from geophysical measurements, particularly in data-sparse regions (Niwas and De
146 Lima, 2003; Singh, 2005; Soupios et al., 2007; Hasan et al., 2021; Asfahani, 2023). In parallel,
147 resistivity-based methods and hydrogeophysical inversion techniques have been developed to
148 more rigorously estimate hydraulic parameters by integrating petrophysical relationships within
149 geophysical modeling frameworks (Daily et al., 1992; Ferré et al., 2009; Binley et al., 2010;
150 Hinnell et al., 2010; Herckenrath et al., 2012; Pollock and Cirpka, 2012; Herckenrath et al.,
151 2013; Binley et al., 2015). These approaches have improved resolution in parameter estimation,
152 particularly in shallow, unconsolidated, or relatively homogeneous settings. However,
153 applications to deep, fractured, and lithologically complex environments remain limited,
154 especially in terms of producing volumetric k models at kilometer-scale depths. Despite these
155 advances, generation of detailed 2D and 3D k maps from resistivity data in deep, hard-rock
156 terrains is constrained by limited borehole control, significant geological heterogeneity, and the
157 ill-posed nature of geophysical inversion. In such contexts, integrating resistivity data with
158 borehole measurements presents a practical, cost-effective solution for characterizing aquifer
159 properties over large areas and depth ranges. This study builds on prior hydrogeophysical

160 | research ~~and by introduces~~ introducing a novel application of the CSAMT method for volumetric
161 k modeling in a complex, fractured hard-rock setting. While previous studies have applied
162 resistivity-based techniques to estimate hydraulic properties, this is the first to utilize CSAMT
163 for constructing the detailed 2D and 3D k modeling beyond 1000 m depth in geologically
164 heterogeneous terrains comprising hornstone, granite, and sandstone. Few available drilling tests
165 were used to calibrate CSAMT-derived resistivity with laboratory-measured k , allowing the
166 resulting empirical relationship to be applied across the broader survey domain. Several CSAMT
167 profiles were conducted along and beyond the borehole locations, and the calibrated resistivity–
168 permeability correlation was used to generate spatially continuous subsurface models in regions
169 lacking direct borehole data. This integration resulted in a robust, data-constrained workflow
170 capable of revealing k variations across diverse rock units and lithological boundaries. The
171 method offers a practical and scalable alternative to extensive drilling campaigns, enabling a
172 more detailed and cost-efficient evaluation of deep groundwater potential in structurally complex
173 terrains.

174 Ultimately, this work extends the scope of hydrogeophysical methods by demonstrating
175 the feasibility of applying CSAMT for deep hydraulic parameter estimation in hard rock. It
176 bridges a critical methodological gap in hard-rock hydrogeology and sets the foundation for
177 future CSAMT-based volumetric modeling in similarly challenging environments. This study
178 aims to develop and apply a geophysical-based approach for mapping the spatial distribution of k
179 in deep, hard-rock settings. By integrating CSAMT data with targeted borehole measurements,
180 this research enhances 2D and 3D hydrogeological assessments across heterogeneous lithologies
181 in structurally complex terrains. It also minimizes reliance on extensive drilling, demonstrating

182 the value of non-invasive geophysical techniques as a cost-effective alternative for deep
 183 groundwater exploration.

184 **Table 1**
 185 Comparative overview of geophysical methods for hydrogeological investigations

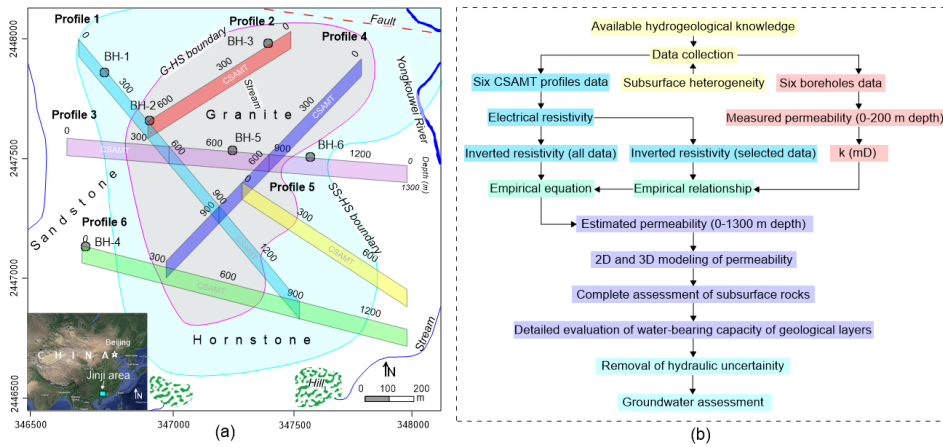
<u>Method</u>	<u>Typical depth of investigation</u>	<u>Spatial resolution</u>	<u>Cultural noise susceptibility</u>	<u>Cost and logistics</u>	<u>Suitability for deep hard rock aquifers</u>
<u>VES (Vertical Electrical Sounding)</u>	<u><200 m</u>	<u>1D only, low lateral resolution</u>	<u>Low–Moderate</u>	<u>Low, rapid</u>	<u>Limited to shallow, homogeneous settings</u>
<u>ERT (Electrical Resistivity Tomography)</u>	<u>Up to ~300 m</u>	<u>High (2D/3D imaging)</u>	<u>Moderate</u>	<u>Moderate; requires dense electrode arrays</u>	<u>Excellent for shallow fractured/karst zones, but inadequate for >500 m depth</u>
<u>TDEM (Time-Domain Electromagnetics)</u>	<u>200–600 m (occasionally deeper)</u>	<u>Moderate</u>	<u>Moderate; affected by near-surface conductivity</u>	<u>Moderate, rapid deployment</u>	<u>Useful for intermediate depths; less effective in highly resistive hard rocks</u>
<u>MT (Magnetotellurics)</u>	<u>Hundreds of m to tens of km</u>	<u>Low in upper crust, improves at depth</u>	<u>High; strongly affected by cultural noise</u>	<u>High; long acquisition times</u>	<u>Excellent for regional mapping and geothermal studies; less suited for site-specific aquifer modeling</u>
<u>CSAMT (Controlled-Source Audio Magnetics Tomography)</u>	<u>~200–1,300 m (depending on frequency)</u>	<u>Moderate–High (2D/3D)</u>	<u>Low; controlled</u>	<u>Moderate; portable,</u>	<u>Well-suited for imaging</u>

Source Audio-
MT) on frequency
& geology) capable) source
minimizes noise adaptable
deep,
resistive,
heterogeneous
aquifers;
strong balance
of depth,
resolution,
and
adaptability

186

187 **2 Methods**

188 This research integrates inadequate/limited drilling information with ~~the~~ geophysical data to
 189 estimate k for both 2D and 3D evaluations of groundwater resources over the entire investigated
 190 site (Fig. 1a). The main stages of the methodology are summarized in the flowchart shown in
 191 Fig. 1b.



192

193 **Fig. 1.** (a) The site map displaying six boreholes (BH-1 to BH-6) and six CSAMT survey profiles (1–6).
 194 The map also illustrates the simplified geological and hydrogeological setting, including the dominant
 195 rock types (granite, hornstone, and sandstone), the granite–hornstone (G–HS) and sandstone–hornstone

196 (SS–HS) boundaries, major fault lines, streams, rivers, and surrounding mountainous terrain; (b)
197 Flowchart illustrating the methodology for generating 2D and 3D k models to enable comprehensive
198 assessments of groundwater resources across extensive areas

199 **2.1 Study area and hydrogeological settings**

200 This study is part of a national initiative in South Guangdong, China, focused on deep
201 subsurface exploration, including groundwater resource assessment and infrastructure
202 development such as the Jiangmen Underground Neutrino Observatory (JUNO) (Hasan et al.,
203 2025). These actions contribute to China's national agenda toward sustainable deep-earth
204 resource utilization. This research was conducted in the Jinji region, a geologically complex area
205 prioritized for deep groundwater exploration (Fig. 1a). The region lies within a subtropical
206 monsoonal climate zone, receiving ~1981 mm of annual rainfall. Topography ranges from low
207 hills to mountainous terrain (39–539.9 m elevation), with dense vegetation and varied slopes.
208 The northern part is relatively flat, while the south includes prominent features such as the
209 Dashishan and Qilongding Mountains. Surface drainage is primarily controlled by the
210 Yongkouwei River in the northeast.

211 Geologically, the Jinji area has evolved through successive tectono-magmatic processes
212 linked to the Yanshanian, Indosinian, and Caledonian mountain-building phases, resulting in a
213 lithologically diverse landscape of granite, sandstone, and hornstone (Qin, 2017). Granite
214 intrusions reflect deep crustal magmatism, while hornstone indicates contact metamorphism.
215 Overlying Paleogene sediments record later basin development. Tectonic structuring in the area
216 is largely influenced by the Kaiping fault-fold complex, which includes reverse, thrust, and
217 strike-slip faults formed under prolonged crustal compression and later modified by strike-slip
218 tectonics. These northeast-trending structures govern subsurface architecture and groundwater

219 flow pathways (Yang et al., 2021). Fractures and joints are widespread in granite, sandstone, and
220 hornstone, varying by lithology and tectonic history. These brittle features act as primary
221 conduits for groundwater, with their alignment along major faults highlighting the tight coupling
222 between structural geology and hydrogeology.

223 This study focuses on the vertical stratification of aquifer-bearing formations. Productive
224 groundwater is mainly stored in deep, fractured sandstone units, overlain by low-permeability
225 granite that limits vertical recharge. An intermediate hornstone layer separates the two, with
226 moderate hydraulic properties and limited connectivity. This configuration isolates the deep
227 aquifer from surface influences, rendering shallow investigations ineffective. Deep-targeted
228 exploration is thus essential for identifying and managing these concealed high-potential
229 groundwater resources in a structurally complex hard rock setting.

230 2.2 CSAMT survey

231 2.2.1 Theoretical background

232 CSAMT is extensively employed for hard rock evaluations due to its ability to resolve deep
233 subsurface features (Fu et al., 2013; Wang et al., 2015; Di et al., 2020; Kouadio et al., 2023).
234 This method employs a distant, regulated electric source that transmits signals into the ground,
235 while electric and magnetic field components are recorded at receiving stations (Zonge and
236 Hughes, 1991). CSAMT uses frequency-dependent EM wave penetration; lower frequencies
237 reach greater depths, depending on rock conductivity (Cagniard, 1953; Borah and Patro, 2019).
238 Signal frequencies are extracted using Fourier transforms from time-series field measurements
239 (Simpson and Bahr, 2005). A typical CSAMT setup uses electric dipole sources arranged

Formatted: Space Before: 1 line, After: 1 line

240 between 1 and 2 km intervals, with 5–10 km offsets based on the required penetration depth and
241 lithological conditions.

242 Resistivity is calculated by analyzing orthogonal electric and magnetic field magnitudes.
243 Vertical resolution typically ranges from 5%–20% of the depth of investigation (DOI), which
244 spans ~20–1000 m. Shallow depths (20–100 m) offer finer resolution, while deeper imaging is
245 coarser due to signal attenuation. DOI increases with lower frequencies and higher subsurface
246 resistivity (Borah and Patro, 2019). Lateral resolution depends on station spacing (10–200 m);
247 wider spacing enhances signal strength and coherence (Simpson and Bahr, 2005). Field setups
248 include portable receivers with electrodes and magnetic sensors to record signals, which are
249 filtered and amplified in real time. Effective survey planning is essential to mitigate interference
250 from fences, power lines, and radio transmitters. Final resistivity models are presented in plan,
251 fence, cross-sectional, or 3D formats.

252 **2.2.2 Survey design and procedures**

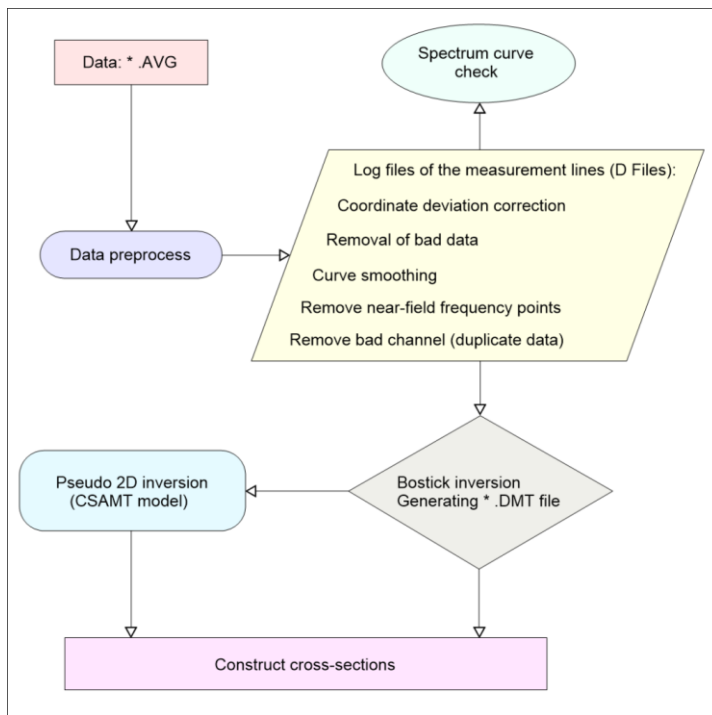
253 Data acquisition was performed along six CSAMT lines (1–6) using a 50 m interval between
254 stations, selected based on geological targets, terrain accessibility, structural orientation,
255 integration with borehole data, and expected resistivity contrasts. These optimized profiles
256 improved subsurface resolution and minimized interpretational ambiguity. The DOI reached
257 approximately 1300 m. Measurements were conducted in scalar Transverse Magnetic (TM)
258 mode, recording E- and H-field vectors in both longitudinal and transverse directions along the
259 survey profiles. EMAP stations were spaced ~50 m from electrodes. A 50 Hz linear filter was
260 implemented under Gain Mode X1 settings. Transmission current spanned 2.6–18 A across the
261 7680 Hz to 1 Hz range.

262 Data acquisition utilized a Phoenix Geophysics V8 multifunction receiver and TXU-30
263 transmitter, capable of 30 kW output, transmitting up to 1000 V and 40 A. The system operated
264 across 34 frequencies (1–7680 Hz), with transmitter–receiver distances of 9.3–12.5 km. Non-
265 polarized electrodes captured electric fields, while magnetic fields were recorded using AMTC-
266 30 sensors (0.1–10,000 Hz). Each site recorded two orthogonal electric and three orthogonal
267 magnetic components, enabling full impedance tensor calculation. Survey positions were
268 determined using Hi-Target V30 RTK and Trimble XH GPS, ensuring sub-meter accuracy.
269 Coordinates were computed and transmitted to the navigation system for real-time positioning.
270 Survey point spacing remained consistent, with system quality metrics indicating 3–5%
271 variability. Design tolerances were met: RMS error $< \pm 5\%$, inter-point error $< 10\%$, horizontal
272 and vertical tolerances of 2.33 mm and 1.67 mm, respectively. Minimal anthropogenic and
273 electrical interference at the site resulted in high-quality data. Final site interpretation was based
274 on rigorous CSAMT data processing, including skew filtering and curve analysis ([Hasan et al.,](#)
275 [2025](#)).

276 **2.2.3 Processing workflow**

277 Spatial filters (Hanning window) and static corrections were applied to refine resistivity data and
278 enhance the model accuracy. The static corrections addressed near-surface resistivity
279 inhomogeneities that cause vertical shifts in apparent resistivity curves. By calibrating electric
280 field measurements to a stable reference, shallow-layer effects were minimized, isolating deeper
281 signals. Spatial filtering using a Hanning window reduced high-frequency noise while preserving
282 coherent spatial patterns. This approach significantly improved inversion model stability by
283 suppressing spectral leakage and smoothing fluctuations. Data processing was carried out using
284 the CMTPro version software produced by Phoenix Geophysics ([Phoenix Geophysics CMTPro](#),

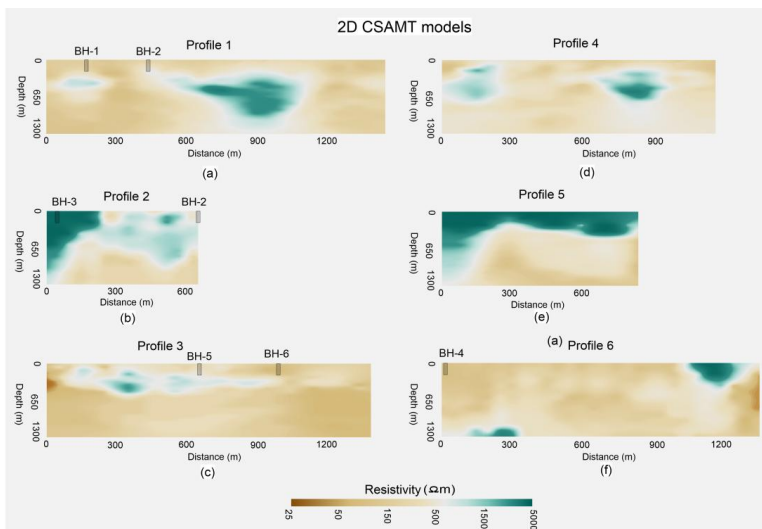
285 2020), which integrates V8 and tracking data, corrects coordinates, smoothes curves, and exports
 286 files for inversion. Based on CSAMT-SW technique, the processing workflow shown in Fig. 2
 287 (Phoenix Geophysics CSAMT-SW, 2020) was conducted to obtain 2D inversion (Rodi and
 288 Mackie, 2001; Wang et al., 2015).



289
 290 **Fig. 2.** Schematic of the 2D CSAMT data inversion workflow using Bostick methodology

291 The main components of the CSAMT-SW framework are: 1. Transformation from AVG
 292 to D format; 2. Editing CHK data and converting to D format; 3. Manual data checks: gap filling,
 293 near-field removal; 4. Smoothing based on D-format data; 5. Estimation of correction factors (D,
 294 H, K, Z); 6. The Bostick inversions; 7. The Quasi-2D inversions using the global field model
 295 (ID), integrating near and transition fields. Post-Bostick inversion results were stored as

296 *_BOS.DAT and *_BSS.DAT, with final inversion-ready data in *_M.DMT. The 2D inversion
297 proceeded until either the RMS error threshold or a five-iteration limit was reached. Final
298 resistivity models (Fig. 3) were cross-validated with local geology and clearly delineated
299 subsurface features, offering a robust interpretation framework.



300
301 **Fig. 3.** Construction of 2D CSAMT models along six geophysical surveyed lines: (a) Line 1, (b) Line 2,
302 (c) Line 3, (d) Line 4, (e) Line 5, and (f) Line 6. Resistivity values increase from brown to green on the
303 color scale.

304 2.3 Permeability estimation framework

305 2.3.1 Laboratory-based permeability determination from borehole core samples

Formatted: Space Before: 1 line, After: 1 line

306 Permeability is a key hydrogeological parameter that quantifies the ability of porous media, such
307 as rock or sediment, to transmit fluids. It governs subsurface fluid flow and plays a central role in
308 groundwater studies (Allègre et al., 2016; Fiandaca et al., 2018; Mudunuru et al., 2022;

309 [Esmailpour et al., 2023](#); [Carbillet et al., 2024](#)). Permeability reflects how easily fluids move
310 through pore networks or fractures and is typically measured via pumping tests or core analysis,
311 methods that are costly and logistically intensive. It is influenced by porosity, lithology,
312 saturation, structural features (e.g., faults, joints), and diagenetic processes ([Dewandel et al.,](#)
313 [2006](#); [Yan et al., 2024](#)).

314 ~~In the present work~~ this study, initial k data from the Jinji region were limited to six
315 boreholes. To strengthen the dataset, 116 lab tests were conducted on core samples from three
316 main lithologies, sandstone (31), hornstone (23), and granite (62), recovered from depths up to
317 200 m. These data help delineate vertical k trends and refine the region's hydrogeological model.
318 Core recovery employed a wireline rotary system with triple-tube barrels to preserve sample
319 integrity ([ISRM, 2015](#)). Samples were vacuum-sealed and stored under controlled humidity to
320 retain in-situ moisture and fracture structure. Prior to testing, cores were trimmed to standard
321 50 mm × 100 mm cylinders and screened for visible defects. Two laboratory methods were used
322 based on k range. The steady-state flow test with ASTM D5084-21 guidelines ([ASTM, 2021](#))
323 was applied to higher- k sandstone. A constant hydraulic gradient was applied under fully
324 saturated conditions, and the corresponding volumetric flow rate was recorded. Permeability was
325 determined through the application of Darcy's Law:

$$326 \quad k = \frac{Q \cdot \mu \cdot L}{A \cdot \Delta P} \quad (1)$$

327 where ΔP shows the pressure differential applied across the sample (Pa), A represents the
328 cross-sectional area (m²), L indicates the length of the sample (m), μ shows the dynamic
329 viscosity of the fluid (Pa·s), and Q denotes the volumetric flow rate (m³/s).

330 For low- k hornstone and granite, the pulse decay method (Brace et al., 1968) was used. A
331 brief pressure pulse was applied, and pressure decay was monitored under confining stresses up
332 to 30 MPa to simulate in-situ conditions and assess stress-dependent k behavior. Tests were
333 conducted under both dry and saturated conditions to evaluate moisture sensitivity. Replicate
334 measurements ensured data reliability, and statistical analyses assessed intra- and inter-lithology
335 variability. Results revealed that granite had the lowest k due to its dense crystalline structure,
336 while hornstone showed intermediate values, likely due to localized fracturing. Sandstone
337 exhibited the highest k , particularly at greater depths, confirming its role as the primary aquifer
338 unit in the region.

339 2.3.2 Permeability-resistivity relationship: Archie's law and the role of Kozeny–Carman

340 Numerous foundational studies have linked electrical resistivity to hydraulic properties like k . A
341 prominent example is the Archie equation (Archie, 1942), which relates resistivity to porosity
342 and water saturation in clean, saturated sediments. However, its assumption of clay-free
343 conditions limits its applicability in complex or clay-rich lithologies (Waxman and Smits, 1968;
344 Glover, 2015). It is commonly expressed as:

$$345 \quad \rho b = a \cdot \rho f \cdot \phi^{-m} \quad (2)$$

346 In this equation, ϕ is porosity, ρf is fluid resistivity, ρb is bulk resistivity, and a and m are
347 empirical constants. Although Archie's law does not directly yield k , porosity serves as a useful
348 proxy due to its strong influence on fluid movement. As such, the resistivity–porosity
349 relationship can be leveraged to infer k indirectly, especially when supplemented with additional
350 petrophysical frameworks (Revil and Cathles, 1999).

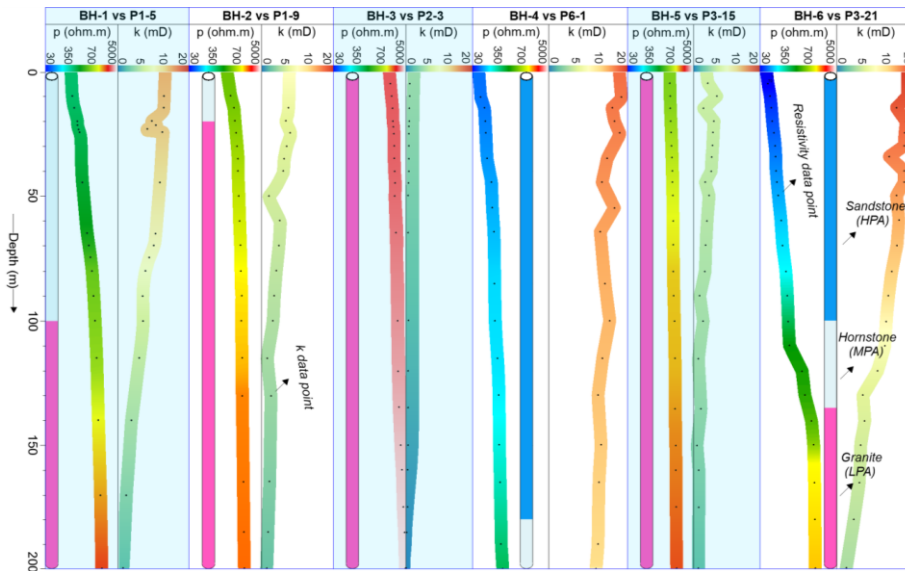
351 The Kozeny–Carman equation, though not used explicitly in this study, provides a widely
352 accepted theoretical foundation that connects k to porosity and specific surface area (DallaValle,
353 1956; Bear, 1972). While it does not incorporate resistivity directly, this model is often used in
354 hydrogeophysical studies to support the interpretation of petrophysical relationships that bridge
355 electrical and hydraulic properties (Chapuis and Aubertin, 2003). Its relevance lies in the broader
356 theoretical justification for using porosity, derived or inferred from resistivity, as a predictor of k .
357 The application of this equation alongside Archie’s law facilitates the development of empirical
358 or semi-empirical models that connect electrical resistivity to k (Glover, 2009; Yan et al., 2024).

359 However, direct application of these equations to complex geological environments, such
360 as fractured granite, sandstone, and hornstone, remains limited due to heterogeneities in mineral
361 composition, pore connectivity, and structural anisotropy. To mitigate such constraints, our
362 approach empirically develops a localized, site-calibrated correlation involving k and resistivity,
363 grounded in co-located deep borehole and CSAMT data. This empirical link supports high-
364 resolution spatial modeling of k in both 2D and 3D for the Jinji area, offering enhanced insight
365 into subsurface hydrogeological conditions where traditional models may not be applicable.

366 2.3.3 Spatial permeability modeling from CSAMT data

367 To estimate permeability across the entire study area, we ~~implemented~~employed a multi-stage
368 approach integrating borehole core analysis with CSAMT-derived resistivity data. In the first
369 stage, a total of 116 laboratory-based k measurements were acquired using 6 drilling tests (from
370 BH-1 to BH-6) with 0–200 m depth (Fig. 4). The k measurements were obtained from intact rock
371 core samples representing three principal lithologies: granite, hornstone, and sandstone.

372 In the second stage, each of the 116 borehole-derived k values was empirically correlated
 373 with corresponding resistivity values extracted from CSAMT soundings co-located with the
 374 borehole sites. The spatial correspondence between boreholes and CSAMT sounding points was
 375 carefully matched (Fig. 4). For example: P1-5 represents the fifth CSAMT sounding at 200 m
 376 along survey line 1 near borehole BH-1; P1-9 corresponds to the ninth sounding at 400 m on line
 377 1 near borehole BH-2; P2-3 denotes the third sounding at 100 m along line 2 near BH-3; P6-1
 378 indicates the first sounding at 0 m on line 6 adjacent to BH-4; P3-15 and P3-21 represent the
 379 fifteenth (700 m) and twenty-first (1000 m) soundings along line 3, near boreholes BH-5 and
 380 BH-6, respectively.



381
 382 **Fig. 4.** Comparison of 116 CSAMT-based resistivity (ρ) data points with corresponding drilling-based
 383 permeability (k) values at depths of 0–200 m across six borehole locations (BH-1 to BH-6). The data were
 384 used to evaluate high potential aquifers (HPA) in sandstone, medium potential aquifers (MPA) in

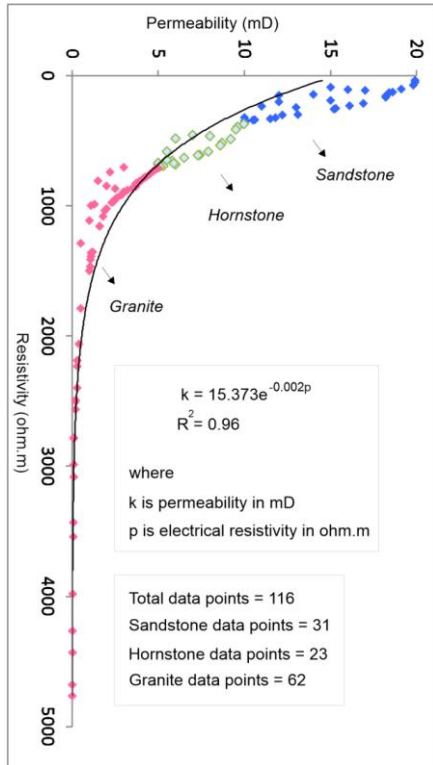
385 hornstone, and low potential aquifers (LPA) in granite. Each dot represents a resistivity or permeability
386 data point. Sounding labels indicate specific CSAMT locations: P1-5 (5th point on line 1), P1-9 (9th on
387 line 1), P2-3 (3rd on line 2), P6-1 (1st on line 6), and P3-15 and P3-21 (15th and 21st on line 3)

388 In the third stage, all 116 paired measurements of k and ρ were utilized to develop an
389 empirical model. An exponential relationship was derived between permeability (k in
390 millidarcies or mD) and electrical resistivity (ρ in Ωm), expressed as follows (Fig. 5):

391
$$k = 15.373 (e)^{-0.002(\rho\rho)} \quad (3)$$

392 This site-specific empirical model was then applied to the entire suite of CSAMT resistivity data
393 collected along six survey profiles to estimate spatial variations in k across the broader study area.
394 Using this relationship, we generated predictive 2D and 3D k models that capture the hydraulic
395 behavior of three major lithological units: low potential aquifer (LPA): associated with low-
396 permeability granite, medium potential aquifer (MPA): hosted within fractured hornstone
397 (hornfels), high potential aquifer (HPA): corresponding to more porous sandstone units.

398 These models provide a depth-resolved assessment of subsurface k reaching depths of up
399 to 1300 m below the surface. Final 2D and 3D spatial visualizations were developed by SKUA-
400 GOCAD and Geosoft Oasis montaj modeling software (Webring, 1981; Mira Geoscience Ltd.,
401 1999; Hasan et al., 2024), enabling the visualization of k distributions across all six CSAMT
402 profiles and improving hydrogeological characterization in structurally complex hard rock terrain.



403

404 **Fig. 5.** Empirical relationship derived from 116 data points comparing CSAMT-based resistivity and
 405 drilling-based k at depths of 0–200 m, across three lithologies: sandstone (31 data points), hornstone (23
 406 data points), and granite (62 data points).

407 **3 Results**

408 **3.1 Cross-validation of geophysical and borehole parameters**

409 [Table 2+](#) summarizes the integrated dataset from 6 drills and 6 geophysical profiles to resolve the
 410 spatial structure of the subsurface into three distinctive hydrogeological units, based on
 411 variations in electrical resistivity and corresponding k values. The development of these

Formatted: Space Before: 1 line, After: 1 line

412 subsurface models mainly depends on borehole data, CSAMT-derived resistivity measurements,
 413 and the regional geological framework. The stratigraphy was categorized into three primary
 414 lithologies: sandstone, hornstone, and granite. Classification criteria were established as follows:
 415 sandstone was defined by resistivity values below 350 Ωm and a k range of 10–20 mD;
 416 hornstone exhibited resistivity values between 350 and 700 Ωm with a k range of 5–10 mD; and
 417 granite was characterized by resistivity values exceeding 700 Ωm and k values ranging from 0 to
 418 5 mD. Based on our evaluations of the subsurface hydrogeological model's aquifer potential
 419 zones, we found that sandstone contains the high potential aquifer (HPA), hornstone contains
 420 medium potential aquifer (MPA), and granite has low potential aquifer (LPA). Aquifers with the
 421 largest yields or the best water-bearing capacity are indicated by sandstone, whereas aquifers
 422 with the lowest yields or the worst water-bearing capacities are denoted by granite. Groundwater
 423 development is best facilitated by sandstone in the study area, whereas groundwater extraction is
 424 most hindered by granite.

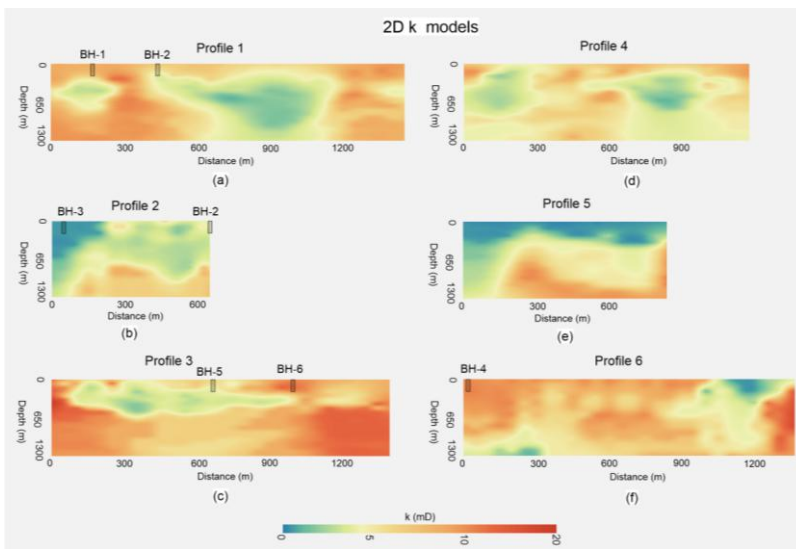
425 **Table 21**

426 Integrating distinct ranges of electrical resistivity and k enables a comprehensive assessment of
 427 groundwater potential across various hard rock types

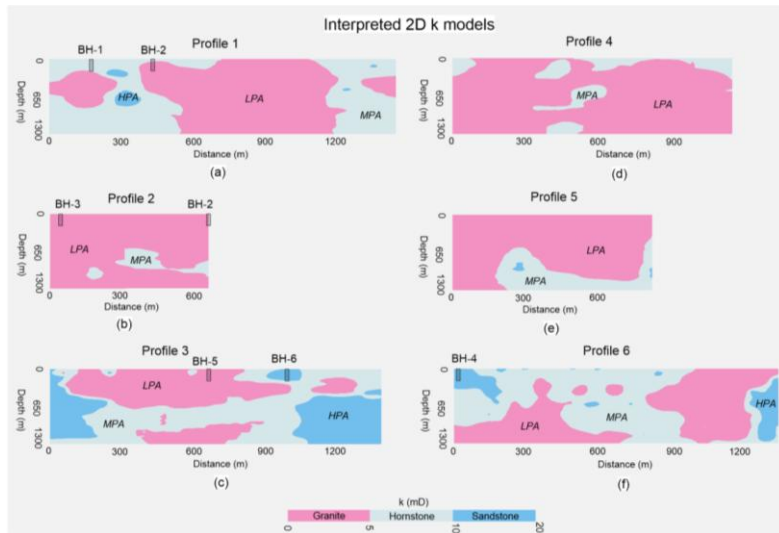
Resistivity (Ωm)	k (mD)	Type of rock	Aquifer potential
< 350	10–20	Sandstone	High potential aquifer (HPA)
350–700	5–10	Hornstone	Medium potential aquifer (MPA)
>700	0–5	Granite	Low potential aquifer (LPA)

428 **3.2 2D groundwater assessments**

429 Using geophysical-borehole correlation as its basis, Eq. (3) efficiently converts 2D CSAMT
430 models (Fig. 3) into 2D k models (Fig. 6). The interpreted 2D k models shown in Fig. 7, in
431 comparison with the limited borehole experiments, allow for a comprehensive assessment of the
432 groundwater resources in hard rock across the whole research area, from 0 to 1300 m deep.



433
434 **Fig. 6.** The predicted 2D k models along six geophysical surveyed lines: (a) Line 1, (b) Line 2, (c) Line 3,
435 (d) Line 4, (e) Line 5, and (f) Line 6. k values increase from blue to red on the color scale.

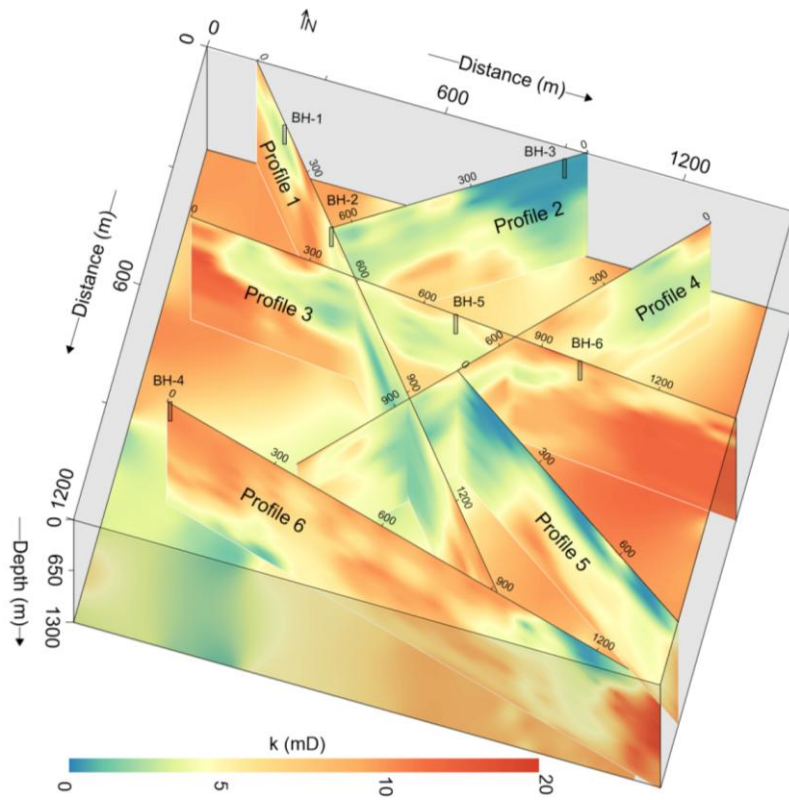


436

437 **Fig. 7.** The interpretation of the predicted 2D k models along six geophysical surveyed lines: (a) Line 1,
 438 (b) Line 2, (c) Line 3, (d) Line 4, (e) Line 5, and (f) Line 6. Sandstone is represented in blue, hornstone in
 439 light blue, and granite in pink

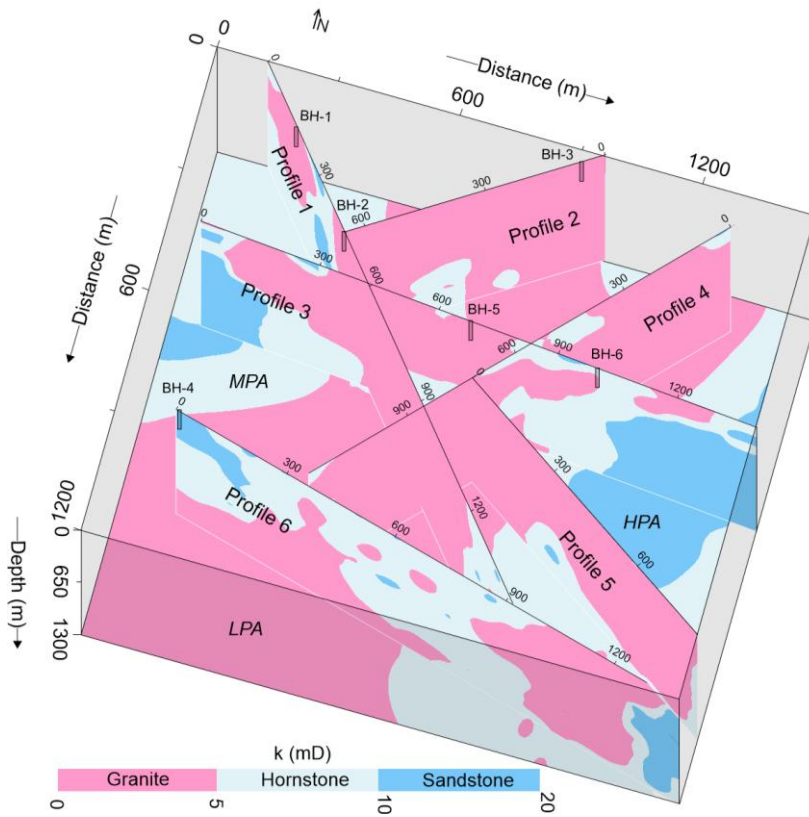
440 The integrated 2D k models (Fig. 8) and their interpretations (Fig. 9) provide a detailed
 441 evaluation of groundwater potential across complex geological settings of sandstone, hornstone,
 442 and granite. Profile 1 reveals a high-potential sandstone aquifer (85–305 m thick) between 245–
 443 380 m distances at 205–400 m depth. Medium-potential hornstone aquifers are found from 0–
 444 525 m and 1185–1445 m distance down to 1300 m. Low-potential granite aquifers appear at 0–
 445 285 m (290–790 m depth), 385–1185 m (full depth), and 1305–1450 m (390–745 m depth).
 446 Profile 2 shows a medium-potential hornstone aquifer with 140–380 m thickness (490–1105 m
 447 depth) between 145–215 m and 290–645 m distance. No high-potential sandstone aquifers are
 448 present. Granite dominates (0–700 m distance, 0–1300 m depth) the profile with low yield except
 449 in hornstone zones. Profile 3 contains both high-potential sandstone (0–250 m, 905–1065 m, and

450 1040–1390 m distances at respective depths of 0–1190, 0–205, and 490–1305 m) and medium-
451 potential hornstone aquifers (full depth with 0–1400 m distance) across the entire surveyed line.
452 Granite aquifers are assessed at 80–1015 m (0–590 m depth), 395–845 m (915–1300 m depth),
453 and 1100–1300 m (200–500 m depth). Profile 4 features medium-potential hornstone at 0–105 m
454 (0–340 m depth), 340–645 m (0 to 1300 m depth), 595–790 m (0–300 m depth), and 1015–1145
455 m (0–345 m depth). No high-potential sandstone is observed. Granite aquifers of low potential
456 dominate (0–1145 m distance between 0–1300 m depth), except in hornstone zones. Profile 5
457 shows medium-potential hornstone (190–845 m distance, 390–1300 m depth) and two small
458 high-yield sandstone patches (290 m at 790–960 m depth and 815 m at 1045–1135 m depth).
459 Low-potential granite appears at distance 0–190 m (0–1300 m depth) and 790–815 m (0–1025 m
460 depth). Profile 6 includes high-potential sandstone zones at 0–190 m (0–490 m depth) and 1245–
461 1345 m (215–1225 m depth). Low-potential granite is present at 0–690 m (390–1300 m depth)
462 and 790–1360 m (0–1190 m depth), while hornstone with medium potential dominates the
463 remainder. Overall, the southeastern and northwestern zones host abundant medium- to high-
464 potential aquifers, while central regions show limited or poor groundwater prospects.



465

466 **Fig. 8.** The integrated 2D k models derived from the incorporation of geophysical and drilling data, with k
 467 represented on a color bar spanning from green to red



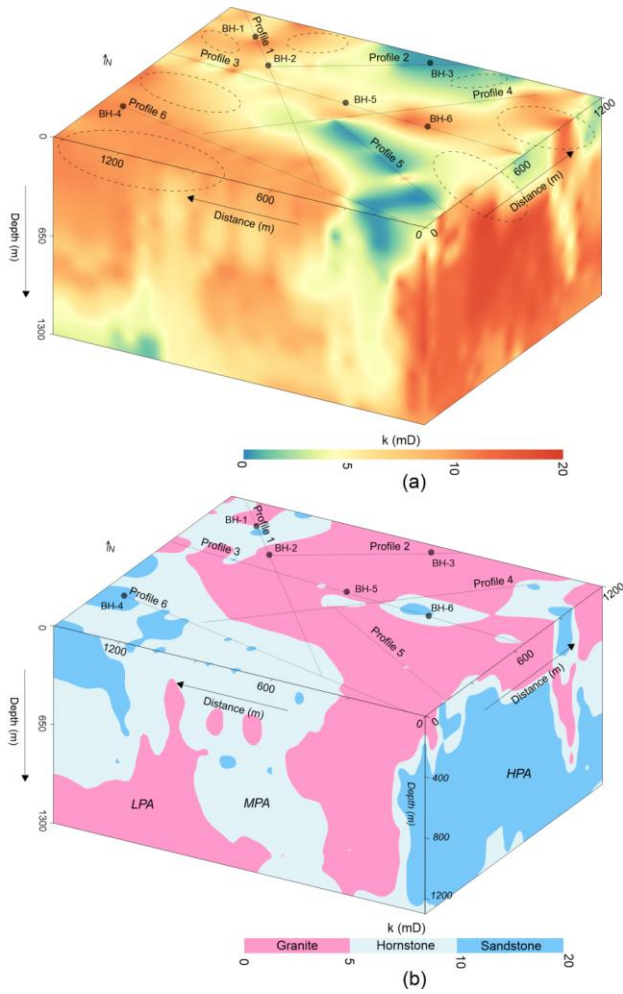
468

469 **Fig. 9** Analysis of 2D k models, based on defined k ranges, for three groundwater potential aquifers: low
 470 potential aquifer (LPA), medium potential aquifer (MPA), and high potential aquifer (HPA),
 471 corresponding to the granite, hornstone, and sandstone formations, respectively

472 **3.3 3D groundwater assessments**

473 The 3D k (outer view) visualization (Fig. 10a, b) provides a comprehensive assessment of the
 474 water-bearing capacity of the rock mass. Low-potential granite aquifers are found at the surface
 475 along: line 1 (85–215 m, 385–1175 m), line 2 (0–655 m), line 3 (0–45 m, 95–175 m, 265–585 m,
 476 605–845 m, 1145–1315 m), line 4 (90–390 m, 490–615 m, 745–1115 m), line 5 (0–815 m), and

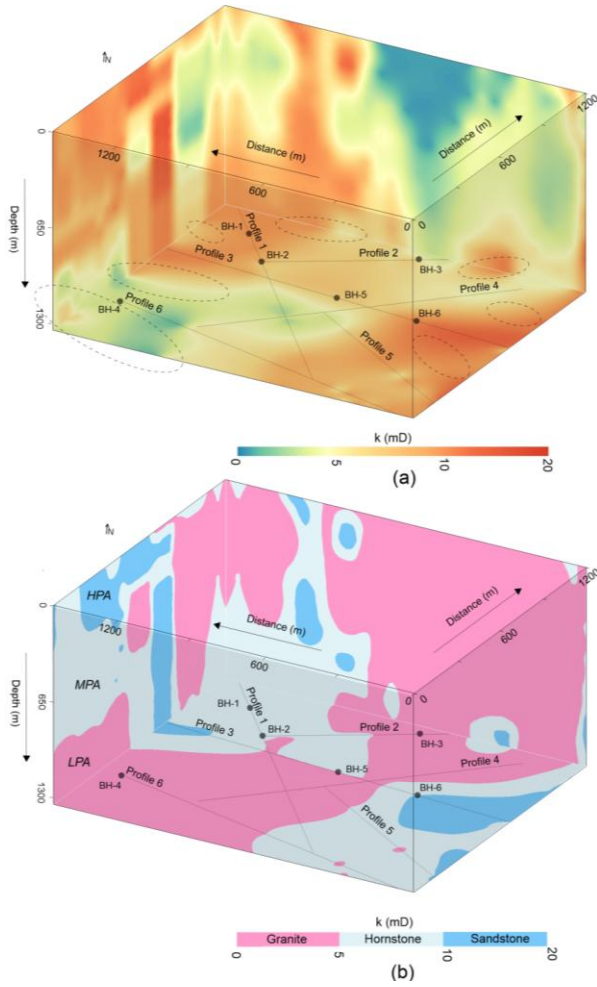
477 line 6 (1045–1345 m). Medium-potential hornstone aquifers appear along: line 1 (0–95 m, 190–
478 260 m, 295–415 m, 1185–1425 m), line 3 (40–105 m, 215–275 m, 580–605 m, 850–910 m,
479 1010–1155 m, 1310–1410 m), line 4 (45–90 m, 390–490 m, 590–685 m, 1115–1185 m), and line
480 6 (90–190 m, 215–275 m, 315–485 m, 505–605 m, 635–1045 m). High-potential sandstone
481 aquifers are identified in: line 1 (265–310 m), line 3 (235–255 m, 915–1010 m), line 4 (0–45 m),
482 and line 6 (0–90 m, 210–225 m, 275–305 m, 515–525 m, 605–635 m). Overall, [Fig. 10 \(a, b\)](#)
483 shows that higher-yield aquifers are mainly concentrated in the southern portion of the
484 investigated site.



485

486 **Fig. 10.** The 3D k models (CSAMT-based), with k shown on a color scale increasing from green to red,
 487 correspond to three groundwater potential aquifers: low potential aquifer (LPA), medium potential aquifer
 488 (MPA), and high potential aquifer (HPA), associated with three geological strata: granite, hornstone, and
 489 sandstone, respectively. The uncertainty contours (highlighted by areas with black dots) indicate zones of
 490 reduced confidence in k estimation. (a) The exterior visualization of the 3D k model, and (b) The analysis
 491 of the 3D k model from an external perspective

492 Fig. 11 (a, b) shows a 3D internal view of aquifer potential at 1300 m depth. Low-yield
493 granite aquifers are identified along: surveyed line 1 (515–1215 m), line 2 (0–290 m), line 3
494 (390–690 m), line 4 (0–1145 m), line 5 (0–195 m, 565–595 m), and line 6 (0–690 m, 1075–1115
495 m). Medium-potential hornstone aquifers are found along: profile 1 (0–540 m, 1215–1445 m),
496 profile 2 (295–675 m), profile 3 (175–395 m, 445–815 m, 915–1035 m), profile 5 (205–565 m,
497 610–815 m), profile 6 (685–1080 m, 1110–1355 m). High-potential sandstone aquifers appear
498 along: profile 3 (0–205 m, 1010–1400 m) and profile 5 (810–815 m). Overall, medium to high
499 potential aquifers are mainly distributed in the southeastern and northwestern regions, while
500 central areas are dominated by low-yield granite. The aerial 3D k model enhances visualization
501 of aquifer distribution, supporting accurate groundwater assessment.



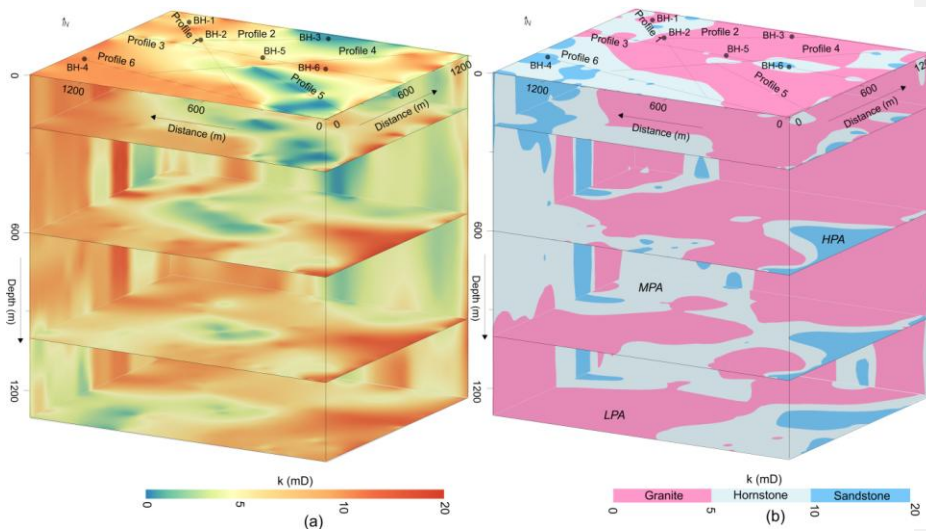
502

503 **Fig. 11.** The 3D k models (CSAMT-based), with k represented on a color scale ranging from green,
 504 illustrate three groundwater potential aquifers: low potential aquifer (LPA), medium potential aquifer
 505 (MPA), and high potential aquifer (HPA), associated with three geological strata: granite, hornstone, and
 506 sandstone, respectively. The uncertainty contours (highlighted by areas with black dots) indicate zones of
 507 reduced confidence in k estimation. (a) The interior visualization of the 3D k model, and (b) The analysis
 508 of the 3D (internal perspective) k model

509 **3.4 Depth-wise groundwater assessments**

510 Due to limited borehole data, direct estimation of k below 200 m is not feasible.
511 However, by integrating borehole and CSAMT data, k values could be reliably estimated down
512 to 1300 m. This approach enabled efficient and detailed evaluation of hard rock aquifers using
513 both 2D and 3D models (Fig. 12), with k values extracted at depths of 0, 200, 600, 1000, and
514 1300 m. At 1300 m, over 42% of the subsurface in the southwest and northeast comprised low-
515 yield granite. Hornstone accounted for 40% (medium yield) near granite zones in the northwest
516 and southeast, while high-yield sandstone made up 18% in the east. At 1000 m, sandstone (15%)
517 was concentrated in the southeast (high yield), hornstone (38%) in the southeast and northwest
518 (medium yield), and granite (47%) dominated the central and boundary zones (low yield). At
519 600 m, the subsurface was 55% granite (central and northern zones, low yield), 32% hornstone
520 (western region, medium yield), and 13% sandstone (southeast, high yield). At 200 m, granite
521 dominated 64% of the center and north (low yield), hornstone made up 26% in the south
522 (medium yield), and sandstone (10%) in the west was associated with high yield. At 0 m, 73% of
523 the central area comprised low-yield granite, 20% of the southwest was hornstone (medium
524 yield), and 7% sandstone (high yield) was concentrated in the southwest.

525 Overall, Fig. 12 shows a decrease in low-yield granite thickness with depth. Groundwater
526 potential is lowest around 600–700 m depth, while deeper zones (>700 m) in the northwest,
527 southeast, and southwest show more favorable aquifer conditions.



528

529 **Fig. 12.** (a) Geophysical k imaging at depths of 0, 200, 600, 1000, and 1300 m, with k shown on a color
 530 scale increasing from green to red. (b) Evaluation of CSAMT-derived k values (based on defined k ranges)
 531 at various depths for different aquifer types: low potential aquifer (LPA) in granite, medium potential
 532 aquifer (MPA) in hornstone, and high potential aquifer (HPA) in sandstone

533 3.5 Validation of predicted vs. measured permeability

534 Groundwater evaluation was greatly improved by systematic CSAMT-based k estimation. As
 535 shown in Figs. 6–12, granite dominates the central, northeastern, and southwestern zones;
 536 hornstone occurs mainly in the southeast, west, and northwest; and sandstone is prevalent in the
 537 east. Borehole-based assessments are limited by inconsistent subsurface mapping. While k values
 538 align near 200 m depth, broader extrapolation remains uncertain, highlighting the limitations of
 539 sparse drilling in complex geology.

540 To clarify the basis of the percentage matching values, the following explicit equation
541 was used to quantify the agreement between CSAMT-derived k' values and borehole-based k
542 estimates:

543
$$\text{Percentage Matching} = \left(\frac{\min(k, k')N_s}{\max(k, k')N} \right) \times 100 \quad (4)$$

544 Here, $\min(k, k')$ is the smaller of the two permeability values, either the measured permeability
545 (k) from borehole data or the estimated permeability (k') from the CSAMT model, at a given
546 depth. Conversely, $\max(k, k')$ is the larger of the two values.~~Here, N_s represents the smaller of the~~
547 ~~two k values, either from the CSAMT model or borehole data, at a given depth, while N is the~~
548 ~~larger.~~ This ratio offers a normalized agreement metric, where 100% indicates a perfect match
549 and lower values reflect greater divergence. Comparisons were made at multiple depth intervals
550 across six calibration boreholes. [Table 32](#) summarizes the percentage agreement for 18 selected
551 data points (out of 116) between measured and predicted k values. Agreement was calculated at
552 matched depth intervals for each borehole–sounding pair using [Eq. \(3\)](#). For example, BH-1 and
553 P1-5 show 73%, 63%, and 100% agreement at 10, 40, and 170 m depth. BH-2 and P1-9 exhibit
554 80%, 77%, and 85% agreement at 20, 60, and 185 m depth. Other pairings, such as BH-3 with
555 P2-3, show lower agreement (67%, 40%, 30%) at 10, 85 and 200 m depth, while BH-5 and P3-
556 15 yield high matches of 80%, 94%, and 85% at 30, 135, and 200 m depth, and BH-6 and P3-21
557 produce matches of 61%, 74%, and 71% at 45, 165, and 180 m depths, respectively.

558 Overall, the results indicate strong consistency between observed and predicted k values,
559 with discrepancies likely due to local heterogeneity or measurement uncertainty. Even at lower
560 percent match, both methods often classify the site into the same aquifer potential zone,
561 supporting the robustness of the CSAMT-based approach for regional groundwater assessment.

562 **Table 32**

563 Percentage match and deviation between the measured k and the predicted k' for 18 selected data points

564 out of the total 116

CSAMT data points (selected)			Drilling data		%Matching	Difference	
CSAMT sounding number	Resistivity (Ωm)	Predicted k' (mD) using Eq. (3)	Borehole name	Depth (m)	Measured k (mD)	k' vs k	between k' and k
P1-5	392	7.0	BH-1	10	9.6	73	2.6
P1-5	515	5.5	BH-1	40	8.7	63	3.2
P1-5	1080	1.8	BH-1	170	1.8	100	0.0
P1-9	669	4.0	BH-2	20	5.0	80	1.0
P1-9	863	2.7	BH-2	60	3.5	77	0.8
P1-9	1354	1.02	BH-2	185	1.2	85	0.18
P2-3	2187	0.2	BH-3	10	0.3	67	0.1
P2-3	2988	0.04	BH-3	85	0.1	40	0.06
P2-3	4765	0.003	BH-3	200	0.01	30	0.007
P6-1	50	13.9	BH-4	15	19.9	70	6.0
P6-1	200	10.3	BH-4	100	12.0	86	1.7
P6-1	348	7.7	BH-4	180	9.9	78	2.2
P3-15	792	3.3	BH-5	30	4.1	80	0.8
P3-15	1157	1.5	BH-5	135	1.6	94	0.1
P3-15	1412	0.91	BH-5	200	1.07	85	0.16
P3-21	165	11.1	BH-6	45	18.2	61	7.1
P3-21	708	3.7	BH-6	165	5.0	74	1.3

P3-21	846	2.8	BH-6	180	2.0	71	0.8
-------	-----	-----	------	-----	-----	----	-----

565

566 **4 Discussion**

567 **4.1 Scalable geophysical approach for deep groundwater modeling**

568 The integration of geophysics into groundwater studies provides an efficient and scalable
569 substitute for borehole-based methods, especially in deep and geologically complex terrains.
570 While boreholes provide direct k data, their use is limited by cost, logistics, and sparse coverage.
571 Our study presents a robust framework for 2D and 3D k modeling beyond 1 km depth by
572 integrating CSAMT with borehole data in a lithologically diverse setting. This approach
573 addresses key challenges in areas with limited surface water and low- k granite near the surface,
574 revealing deeper fractured zones with higher groundwater potential in granite, hornstone, and
575 sandstone. These deep aquifer insights support China's national water security strategies and
576 inform sustainable groundwater management under climate stress.

577 **4.2 Ensuring data quality and model reliability**

578 To minimize uncertainty and enhance accuracy, we implemented a rigorous workflow
579 throughout data acquisition, processing, inversion, and modeling. For CSAMT, this included
580 careful survey planning, optimized electrode configurations, and the application of advanced
581 filtering and static shift corrections. Inversion was guided by multidimensional modeling
582 constrained by borehole-derived a priori information, improving resolution and mitigating non-
583 uniqueness. Permeability measurements were obtained under controlled laboratory conditions
584 using high-quality, undisturbed core samples from six boreholes, reducing discrepancies between

Formatted: Space Before: 2 line, After: 1 line

585 laboratory and field scales. These measures, together with integrated lithological data, enabled
586 the development of a robust k model suitable for reliable groundwater assessment across the
587 study area.

588 **4.3 Comparative advantages of CSAMT for deep hard rock aquifer characterization**

589 CSAMT, developed in the 1970s, remains uniquely valuable for deep subsurface exploration,
590 particularly in resistive and fractured hard rock environments. Its ability to image at
591 intermediate-to-deep depths (hundreds to over a thousand meters) with relatively high resolution
592 and controlled signal strength enhances its ability to delineate lithological contacts and fluid-
593 bearing formations where other resistivity methods (VES and ERT) may fall short. While
594 electromagnetic methods such as MT and TDEM are also capable of probing deep subsurface
595 structures, achieving comparable results in similarly complex hard rock settings presents notable
596 challenges. MT, which relies on natural variations in electromagnetic fields, can reach even
597 greater depths than CSAMT and has been successfully applied in regional-scale hydrogeological
598 investigations, such as identifying deep groundwater circulation paths in mountain systems
599 (Jiang et al., 2014) and tracing flow systems that recharge lowland aquifers (Gonzalez-Duque et
600 al., 2024).

601 ~~However, MT's lower resolution in the upper crust and dependency on natural field~~
602 ~~conditions often limit its effectiveness in detailed, site-specific k modeling, particularly when~~
603 ~~borehole calibration is sparse. Similarly, TDEM is widely used for near surface to intermediate-~~
604 ~~depth investigations and offers rapid deployment, but its signal strength and resolution tend to~~
605 ~~decrease in highly resistive formations, making it less suitable for imaging deep, fractured zones~~
606 ~~in hard rock. Therefore, while MT and TDEM are powerful methods for broad scale~~
607 ~~groundwater assessment, they are less suited to the high resolution, volumetric modeling of k in~~

608 varied lithologies beyond 1km depth. In contrast, CSAMT's controlled source design, moderate-
609 to deep depth penetration, and strong signal to noise ratio in resistive environments make it
610 better aligned with the goals of this study. The approach bridges the gap between large scale
611 geophysical surveys (e.g., MT or TDEM) and localized drilling, enabling spatially continuous
612 2D and 3D hydrogeophysical models essential for evaluating deep aquifer potential. While MT
613 or TDEM may complement such studies at regional scales, achieving this level of resolution and
614 lithological detail in a hard rock context currently remains more feasible with CSAMTAs
615 summarized in Table 1, MT provides exceptional penetration (tens of kilometers) but has
616 reduced resolution in the upper crust and is highly sensitive to cultural noise, limiting its
617 suitability for detailed *k*-modeling at the site scale. TDEM, while rapid and effective for
618 intermediate depths, suffers loss of sensitivity in highly resistive formations, making it less
619 effective for fractured granite and hornstone settings. In contrast, CSAMT's controlled-source
620 design and strong immunity to cultural noise provide a balance of depth penetration and
621 resolution well-suited for site-specific groundwater studies in hard rock terrains.

Formatted: Font color: Light Blue

622 Thus, the comparative analysis (Table 1) underscores why CSAMT is the most
623 appropriate method for this study: it bridges the gap between large-scale regional techniques
624 (MT, TDEM) and shallow, high-resolution methods (VES, ERT), enabling robust 2D and 3D
625 hydrogeophysical modeling essential for evaluating deep aquifer potential.

Formatted: Font: Not Bold, Font color: Light Blue

626 4.4 Calibrated resistivity thresholds for lithological and hydraulic discrimination

627 We developed a robust empirical relationship between resistivity and *k* using 116 co-located data
628 pairs, 62 from granite, 31 from sandstone, and 23 from hornstone, spanning 35–4,765 Ωm and
629 0.01–19.9 mD, respectively. The strong correlation ($R^2 = 0.96$) ensures reliable *k* prediction and
630 minimizes lithological bias. The lithological classification derived from the resistivity–

631 permeability relationship in this study is both geologically plausible and empirically supported
632 by borehole data and field observations. Specifically, granite showed high resistivity ($>700 \Omega\text{m}$)
633 and low k (0–5 mD), hornstone had intermediate resistivity (350–700 Ωm) and moderate k (5–
634 10 mD), and sandstone was marked by low resistivity ($<350 \Omega\text{m}$) and higher k (10–20 mD).
635 These ranges align with the distinct hydrogeological behaviors of each lithology under the site-
636 specific structural and mineralogical conditions. The resistivity thresholds were selected through
637 an integrated approach combining lithological logs from boreholes, established empirical
638 resistivity values reported in the literature, and the geoelectrical contrasts identified in CSAMT
639 profiles. For instance, the high resistivity of granite reflects its dense, low-porosity matrix and
640 limited fluid content, whereas the lower resistivity of sandstone and hornstone corresponds to
641 increased pore connectivity and higher saturation, often ~~enhanced by associated with~~ structural
642 features or thermal alteration. To ensure robust classification, the resistivity thresholds were
643 calibrated using co-located borehole observations from multiple calibration sites and iteratively
644 refined to maximize agreement between observed lithology and the modeled resistivity–
645 permeability domains. While we acknowledge that resistivity can vary within a given lithology
646 due to localized factors such as fluid saturation, mineral alteration, or fracture density, sensitivity
647 analyses indicated that moderate adjustments to the threshold values had minimal impact on the
648 overall lithological classification or the interpretation of k trends. This suggests that the chosen
649 thresholds are well-suited to the structurally complex Jinji area. Nevertheless, we emphasize that
650 these resistivity–permeability associations are localized and should be recalibrated to account for
651 site-specific conditions before use elsewhere. Although site-specific, the approach demonstrates
652 how minimal calibration data can support high-resolution 2D/3D k modeling in data-scarce

653 settings. Future studies could benefit from probabilistic classification schemes or machine
654 learning approaches to further refine lithological mapping in geologically heterogeneous terrains.

655 **4.5 Impact of lithological and measurement variability on the resistivity–permeability** 656 **relationship**

657 The fitted relationship between resistivity and k , as illustrated in Fig. 5, is shaped by several
658 factors, including the geological setting, lithological heterogeneity, data distribution, and the
659 accuracy of both measurements. The broad dynamic range in our dataset provides a strong basis
660 for identifying trends across the three dominant lithologies: sandstone, granite, and hornstone.
661 This broad range is especially beneficial for resolving low- k formations such as granite, where k
662 remains uniformly low and shows minimal fluctuation. In these settings, even large shifts in
663 resistivity translate to relatively small changes in k , resulting in a gently declining inverse
664 relationship. In contrast, at lower resistivity values (e.g., $<1,000 \Omega\text{m}$) where k exceeds 2 mD,
665 small resistivity shifts result in larger changes in k , leading to a more scattered and nonlinear
666 correlation. This pattern is geologically realistic and reflects the inherent variability of fractured
667 and porous zones in complex lithologies.

668 **4.6 Model validation and predictive reliability**

669 Matching between measured and predicted permeability (k vs. k') was also rigorously validated
670 (Table 32). Among 18 selected points from boreholes, 10 showed a difference of less than 1 mD,
671 with only two exceeding 4 mD. Despite minor deviations, all points were accurately classified by
672 lithology. This confirms the empirical model's reliability and its utility for regional-scale k
673 prediction, even in areas lacking direct measurements. The geophysical model effectively

674 compensates for sparse drilling data, offering a scalable and cost-effective tool for
675 hydrogeological evaluation in hard rock terrains.

676 **4.7 Limited and shallow borehole calibration**

677 A key limitation of this study lies in the depth extent of the calibration dataset. The empirical
678 resistivity-permeability relationship was developed using 116 core samples from six boreholes,
679 all restricted to depths between 0 and 200 m. Extrapolating this relationship to 1300 m depth
680 introduces uncertainty, as no direct calibration exists at greater depths. To address this limitation,
681 we incorporated a probabilistic modeling framework that quantifies the increase in uncertainty
682 with depth. The model results (Fig. 13) clearly illustrate that while near-surface permeability
683 estimates are relatively well constrained, the confidence intervals expand significantly beyond
684 ~200 m due to the lack of direct sampling.

685 Future work should therefore prioritize the acquisition of deep borehole data (>500 m),
686 including core sampling, hydraulic pumping tests, and packer testing, to directly validate the
687 extrapolated permeability values. In addition, the integration of advanced downhole geophysical
688 logging with geostatistical and probabilistic approaches will provide stronger constraints on
689 subsurface heterogeneity at depth. Such efforts will be essential to improve confidence in deep
690 permeability predictions, reduce geological uncertainty, and enhance the reliability of
691 groundwater resource assessments in complex crystalline terrains.

692 **4.8.7 Choice of core-based permeability measurements versus pumping tests**

693 Although pumping tests are widely regarded as the standard method for estimating aquifer
694 permeability (k), they provide only bulk, large-scale averages of hydraulic conductivity over the
695 tested interval. Such measurements are useful for assessing overall transmissivity but lack the

696 spatial resolution required for detailed 2D or 3D geophysical modeling, where localized contrasts
697 in hydraulic properties are critical. The objective of this study was to capture subsurface
698 heterogeneity at scales compatible with CSAMT-derived resistivity. For this purpose, point-
699 specific k measurements were necessary to ensure that calibration data reflected the same
700 resolution and spatial variability represented in the geophysical models. Core samples, analyzed
701 at discrete depths, offered this localized control and provided a closer match to the spatial scale
702 of CSAMT blocks. Therefore, core-derived k values were used in lieu of pumping tests. While
703 this approach inevitably shifts the focus from bulk aquifer transmissivity to matrix- and fracture-
704 scale variability, it ensures that the calibration dataset is scale-compatible with resistivity
705 measurements, thereby improving the reliability of the empirical k - ρ relationship and supporting
706 more accurate heterogeneity mapping in crystalline terrains.

707 **4.9 Scale effects in permeability estimation**

708 While core plug measurements and CSAMT-derived resistivity are broadly compatible for
709 establishing an empirical k - ρ relationship, it is important to acknowledge the differences in
710 sampling scale. Core-derived permeability (k) values, measured on centimeter-scale samples,
711 largely capture matrix properties of the rock. These may underestimate flow capacity where
712 nearby fractures or heterogeneities are missed. In contrast, CSAMT inversions, with an effective
713 resolution of $\sim 50 \times 50$ m, represent a bulk effective property that integrates both matrix and
714 fracture contributions across larger volumes.

715 This scale difference provides a natural explanation for the scatter observed in the k - ρ
716 dataset (Fig. 5). For example, a core extracted from intact granite may record low k , while the
717 corresponding CSAMT block encompasses a fracture corridor that increases the effective k .
718 Conversely, a core intersecting a fracture may yield anomalously high k compared to the

719 surrounding bulk medium resolved by CSAMT. Thus, while the fine-scale core data were
720 essential for establishing point-specific calibration with resistivity values, the observed scatter
721 reflects the complementary strengths of the two approaches: core testing constrains intrinsic rock
722 matrix properties, and CSAMT captures fracture-controlled heterogeneity and connectivity at the
723 field scale. Together, they provide a more robust characterization of hydraulic behavior than
724 either method alone. Future work should strengthen this multi-scale integration by including
725 intermediate-scale datasets such as borehole geophysics and aquifer-scale pumping tests. Such
726 efforts would further bridge the gap between matrix-scale and bulk-scale measurements,
727 reducing uncertainty in k modeling for complex crystalline terrains.

728 **4.108 Inflection in the resistivity–permeability relationship: a depth analogue**

729 The empirical resistivity–permeability (k – ρ) relationship developed in this study exhibits a sharp
730 decline in k with increasing resistivity and a clear inflection near 1,000 Ωm . This mirrors classic
731 depth–permeability (k – z) trends (e.g., Manning and Ingebritsen, 1999; Saar and Manga, 2004;
732 Ingebritsen and Manning, 2010), where k decreases exponentially at shallow depths and follows
733 a power-law pattern deeper down. However, unlike those models that use depth alone, our
734 resistivity-based approach captures additional controls such as lithology, porosity, fluid content,
735 and fracturing, making it a more localized and physically representative proxy, especially in
736 heterogeneous hard rock settings.

737 Depth was considered but not used as the primary variable due to strong lateral variations
738 in resistivity and k caused by geological complexity. For instance, in the Jinji area, surface
739 granite shows high resistivity and low k , consistent with standard crustal profiles. However,
740 deeper hornstone and sandstone units exhibit lower resistivity and higher k , contrary to typical
741 depth trends, likely due to localized faulting, thermal alteration, and contact metamorphism that

742 enhance fracture connectivity. The resemblance between our k - ρ curve and established k - z
743 models reinforces its physical validity. The observed transition near 1,000 Ωm may reflect a shift
744 from conductive, fractured zones to compact, resistive rock masses. While hybrid models
745 incorporating depth may be useful in future work, our resistivity-based method provides a more
746 reliable and site-specific approach for k estimation in structurally complex terrains.

747 **4.119 Salinity effects and ~~limitations of deep calibration~~ uncertainty in deep fluid**
748 **properties**

749 The influence of factors beyond lithology, particularly groundwater salinity, on CSAMT-derived
750 resistivity warrants consideration. Electrical resistivity is inherently sensitive to porosity, fracture
751 density, mineral alteration, fluid saturation, and salinity. In this study, k calibration was based on
752 core samples from 0–200 m depths across six boreholes. While this limits direct calibration at
753 greater depths, hydrochemical data from the Geological Survey of China, spanning 800–1,000 m
754 depth, consistently indicate fresh groundwater, suggesting salinity is not the cause of deeper low-
755 resistivity zones. We interpret these zones, especially in sandstone and hornstone, as reflecting
756 high saturation and pore connectivity rather than saline fluids. This is further supported by the
757 absence of resistivity anomalies typically associated with brackish water, and the strong
758 alignment between resistivity, k , and lithological boundaries. ~~However, due to the lack of salinity~~
759 ~~data below 1 km, the role of deep fluid conductivity cannot be fully ruled out, a limitation of the~~
760 ~~current study. Future work should include deep borehole sampling and in situ fluid logging to~~
761 ~~better constrain this relationship.~~

762 However, because no fluid data are available below 1 km, the role of salinity cannot be
763 entirely excluded, representing a key assumption and limitation of this study. A sensitivity

764 analysis indicates that if fluid resistivity (ρ_f) were halved due to salinity, the apparent formation
765 resistivity (ρ) would decrease by ~50%. Substituting this reduced resistivity into our resistivity–
766 permeability relationship (Eq. 3) yields higher permeability (k) values, as k increases
767 exponentially with decreasing ρ . Specifically, halving ρ_f would increase inferred k by
768 approximately a factor of 2 at 1000 Ωm , 7 at 2000 Ωm , and 18 at 3000 Ωm . These results
769 demonstrate that salinity effects are modest at shallow depths but may become significant at
770 greater depths. Future investigations should therefore incorporate deep borehole sampling, fluid
771 logging, and hydrochemical analyses to directly constrain fluid resistivity and reduce uncertainty
772 in k extrapolation.

773 **4.120 Model construction and uncertainty in 3D permeability mapping**
774 **Uncertainty from model extrapolation and edge effects**

775 ~~The 3D k model was developed by interpolating between 2D CSAMT inversion profiles~~
776 ~~calibrated with borehole derived k from six reference locations. Due to limitations in survey~~
777 ~~geometry and computational cost, full 3D inversion was not feasible. Instead, a geostatistical~~
778 ~~framework using ordinary kriging integrated cross sections and applied the resistivity–~~
779 ~~permeability relationship across the volume, constrained by lithological boundaries and borehole~~
780 ~~data. While this approach provides a volumetric view of k , model reliability declines toward the~~
781 ~~edges and corners where data density is limited. Sensitivity analyses, based on variogram~~
782 ~~adjustments and comparisons of interpolation algorithms, revealed elevated uncertainty in these~~
783 ~~peripheral zones. To convey this, uncertainty contours were added to the 3D figures (Figs. 10~~
784 ~~and 11), delineating areas of reduced confidence. The model's core, where CSAMT lines~~
785 ~~intersect and borehole constraints exist, offers the highest reliability. Boundary regions should be~~

786 ~~interpreted with caution. Future work with denser CSAMT coverage or full 3D inversion would~~
787 ~~enhance model accuracy and reduce edge-related uncertainties.~~

788 The 3D permeability (k) model was constructed by interpolating between 2D CSAMT inversion
789 profiles calibrated with borehole-derived k values from six reference locations. Given the
790 limitations in survey geometry and computational cost, full 3D inversion of the resistivity data
791 was not feasible. Instead, we implemented a geostatistical framework using ordinary kriging,
792 which integrated cross-sectional profiles and applied the resistivity–permeability relationship
793 across the model volume. The interpolation was guided by variogram models tuned to reflect the
794 spatial continuity of lithological units and constrained by borehole control points, thereby
795 maintaining geological consistency. While this approach provides a volumetric representation of
796 k that highlights the distribution of permeable zones, its reliability is scale- and data-density
797 dependent. The model is most robust in the central areas where CSAMT lines intersect and are
798 directly supported by borehole data. In contrast, reliability diminishes in regions between widely
799 spaced profiles and toward the model edges and corners, where no direct constraints exist.
800 Sensitivity analyses, based on alternative variogram structures and comparisons with inverse
801 distance weighting, consistently revealed greater variability and uncertainty in these peripheral
802 zones.

803 To address this, uncertainty contours were added to Figs. 10 and 11, delineating areas of
804 higher and lower confidence. The black dots marking borehole and survey line positions serve as
805 reference anchors, making it clear that interpolation quality decreases with increasing distance
806 from these control points. As such, interpretations in boundary regions should be treated with
807 caution, particularly where model predictions extend beyond the convex hull of available data.
808 We emphasize that the current model provides a reliable first-order framework for k distribution

Formatted: Font: Not Bold, Italic

809 in the study area, but future improvements should prioritize denser CSAMT line coverage and,
810 where feasible, the use of full 3D inversion techniques. Such approaches would better capture
811 lateral continuity, minimize edge effects, and enhance confidence in the extrapolated 3D
812 structure.

813 **4.1.31 Limitations of storage characterization**

814 A complete groundwater assessment requires evaluating both k and storage parameters. This
815 study focused on delineating spatial variations in k , referred to here as “water-bearing capacity”;
816 using CSAMT-derived resistivity calibrated with borehole data. A complete aquifer assessment
817 requires evaluation of both permeability (k) and storage parameters such as storativity, specific
818 yield, and specific storage. This study focused primarily on delineating spatial variations in k ,
819 referred to here as “water-bearing capacity,” using CSAMT-derived resistivity calibrated with
820 borehole data. While this approach provides valuable insights into transmissivity and flow
821 potential, it does not directly constrain aquifer storage capacity.

822 While we emphasize k , we acknowledge that key storage parameters such as porosity,
823 specific yield, and specific storage remain unmeasured due to the absence of deep aquifer tests
824 and formation logs. However, geological and geophysical evidence allows for qualitative
825 inference. Due to the absence of deep pumping tests and detailed formation logs, storage
826 parameters could not be quantified. Instead, our interpretations rely on qualitative geological and
827 geophysical inference. Permeable units like sandstone and hornstone likely possess higher
828 porosity due to their granular textures and fracture networks, unlike the denser granite. This is
829 supported by groundwater level data from six boreholes and regional water table records, which
830 indicate aquifers in fractured, low-resistivity zones. These zones align spatially with permeable

Formatted: Font: Not Bold, Font color: Red

831 features in both CSAMT/ k models and borehole data. ~~Our current interpretation focuses on~~
832 ~~relative transmissivity, not absolute storage capacity, a limitation we acknowledge. Future work~~
833 ~~should include porosity and storage measurements through deep borehole testing, in situ logging,~~
834 ~~and hydraulic analysis to support more comprehensive aquifer characterization in complex hard~~
835 ~~rock settings.~~

836 We acknowledge that the current study characterizes relative transmissivity rather than
837 absolute storage capacity, representing a key limitation. Future work should therefore integrate
838 porosity and storage characterization through deep borehole testing, in-situ hydrochemical and
839 geophysical logging (e.g., nuclear magnetic resonance), and aquifer hydraulic analysis to provide
840 a more comprehensive basis for groundwater resource evaluation in complex hard rock terrains.

841 **4.1.4.2 Optimizing borehole placement for CSAMT calibration**

842 Borehole placement in this study was strategically guided by geological mapping, hydrological
843 relevance, and preliminary geophysical data to ensure representative coverage of key lithologies
844 and structures. These boreholes served both to calibrate resistivity–permeability relationships
845 and to validate the CSAMT-derived k models. While there's no fixed number of required
846 boreholes, our results show that a small but well-distributed set across major lithological and
847 structural zones yields reliable model performance. A leave-one-out validation confirmed that
848 the model maintains coherent spatial trends, though with slightly reduced accuracy in
849 geologically complex areas. This highlights both the importance of strategic calibration point
850 distribution and the robustness of the CSAMT-based approach, even with limited borehole data.
851 Future efforts could improve efficiency by adapting borehole placement based on preliminary
852 CSAMT results, optimizing both calibration and cost.

853 **4.1.53 Rationale for variable CSAMT profile extents**

854 The variation in CSAMT profile lengths reflects site-specific logistical and geological
855 constraints encountered during field deployment. Factors such as terrain accessibility,
856 infrastructure (e.g., roads, buildings), and the need to capture key geological features (e.g., faults,
857 lithological boundaries) influenced the extent of each profile. In some cases, shorter profiles
858 were required due to rugged topography or land access limitations, while longer profiles were
859 employed where feasible to ensure adequate coverage across broader structural domains. Despite
860 the variation in length, all profiles were designed to achieve sufficient depth penetration and
861 resolution for reliable resistivity–permeability modeling, as validated through borehole
862 calibration.

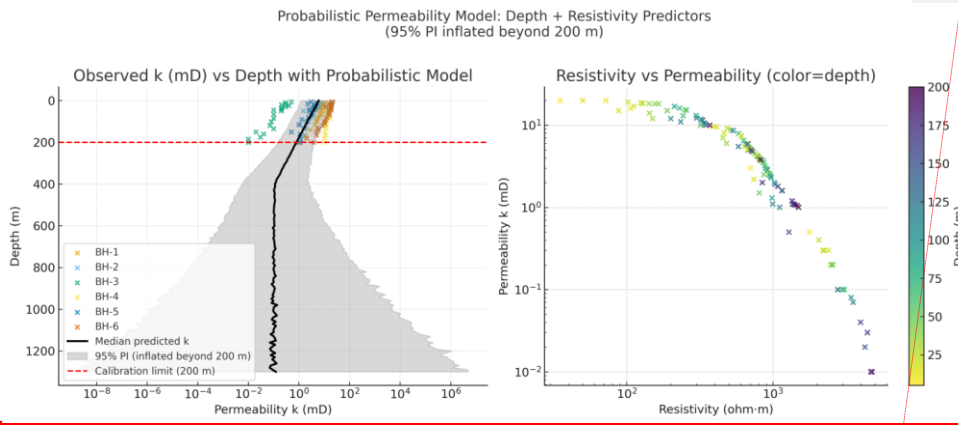
863 **4.1.64 Addressing the borehole–CSAMT depth discrepancy**

864 Although the borehole data used for calibration were limited to depths of 0–200 m, this interval
865 encompasses key lithological units, granite, hornstone, and sandstone, and captures a
866 representative range of resistivity and k conditions. These near-surface measurements provided a
867 robust basis for developing the empirical resistivity–permeability (k – ρ) relationship, which was
868 subsequently applied across the full depth range of the CSAMT profiles (~1300 m). While direct
869 validation at greater depths is not currently possible due to the absence of deep borehole data, the
870 extrapolation of the calibrated model is supported by consistent geological structure,
871 hydrochemical data, and stratigraphic continuity reported by the Geological Survey of China
872 down to ~1000 m. Furthermore, strong spatial alignment between resistivity, inferred k , and
873 mapped lithological boundaries lends confidence to the model's deeper projections. We
874 acknowledge this depth mismatch as a limitation, but emphasize that the approach enables

875 meaningful k estimation in data-scarce regions. Future studies incorporating deep drilling and in-
876 situ petrophysical logging will be essential to further refine model accuracy at greater depths.

877 4.175 Ground-truthing CSAMT with regional geological frameworks

878 Our results show strong agreement with regional geological and hydrogeological data from local
879 and national surveys, confirming the reliability of the integrated CSAMT–borehole approach.
880 This alignment supports the method’s scientific validity and scalability for k estimation in
881 structurally complex, data-scarce settings. While grounded in established geophysical principles,
882 the strength of this study lies in its site-specific integration of deep k modeling, field validation,
883 and empirical calibration. Overall, the findings highlight CSAMT’s potential as a practical tool
884 for deep groundwater exploration and sustainable resource management.



885

886 **Fig. 13.** Probabilistic permeability–depth model based on resistivity–permeability calibration from 116
887 borehole samples (0–200 m). The extrapolation to 1300 m shows increasing uncertainty with depth due to
888 limited calibration data.

Formatted: Font: Not Bold

Formatted: Left, Space Before: 1 line, After: 1 line

Formatted: Font: Bold

889 **5 Conclusions**

890 This study introduces a novel, non-invasive methodology for deep groundwater investigation
891 using CSAMT, applied for indirect estimation of 2D and 3D k distributions in complex hard rock
892 terrains at depths reaching 1300 m. Conventional borehole drilling remains indispensable for
893 direct hydraulic parameter evaluation, but its high cost and limited coverage restrict broader
894 applicability. Our approach combines borehole calibration with CSAMT resistivity to establish
895 an empirical k - ρ relationship, enabling the construction of spatially continuous hydrogeological
896 models that extend beyond the reach of direct sampling.

897 It is important to note that the empirical relationship (Eq. 3) derived in this study is site-
898 specific to the Jinji region's geological and hydrogeochemical conditions. Its constants should
899 not be generalized to other regions without new calibration data. The key contribution of this
900 work is therefore the methodology, a workflow for integrating CSAMT with borehole
901 calibration, rather than the specific coefficients of the empirical equation. The resulting
902 permeability models align well with lithological boundaries, revealing low- k granite zones (>700
903 Ωm , 0–5 mD) and high- k sandstone zones ($<350 \Omega\text{m}$, 10–20 mD). Promising groundwater
904 targets were identified below 700 m in central regions and around granite–sediment contacts,
905 extending to depths of ~ 1300 m. While these results demonstrate the power of CSAMT for deep
906 groundwater assessment, they remain dependent on the availability and quality of borehole data
907 for calibration.

908 Future work should emphasize deep borehole validation, probabilistic modeling, and
909 multi-scale integration to reduce uncertainty and improve confidence in permeability predictions.
910 By coupling CSAMT with hydrochemical, porosity, and advanced logging data, this approach

911 can evolve into a robust and transferable framework for groundwater assessment in complex
912 hard rock terrains, while acknowledging inherent site-specific limitations.

913 **Code availability**

914 Software application or custom code supports the published claims and complies with field
915 standards

916 **Data availability**

917 Data available on request from the corresponding author

918 **Author contributions**

919 MH conceptualized the research goals and developed the methodology. MH and LS found the
920 funding for the project. MH developed the code and prepared its visualization, and LS provided
921 programming support and analysis tools. MH prepared the original draft.

Formatted: Space Before: 1 line

922 **Declaration of competing interest**

923 The authors declare that they have no conflict of interest.

Formatted: Space Before: 1 line, After: 1 line

924 **Acknowledgements**

925 The authors gratefully acknowledge the support provided by the State Key Laboratory of
926 Mountain Hazards and Engineering Resilience, Institute of Mountain Hazards and Environment,
927 Chinese Academy of Sciences, and the China-Pakistan Joint Research Center on Earth Sciences,
928 CAS-HEC, Islamabad, Pakistan.

929 **Financial support**

930 This research was financially supported by the National Natural Science Foundation of China
931 (Grant No. U22A20603), the International Science and Technology Cooperation Program of
932 Shanghai Cooperation Organization, Science and Technology Department, Xinjiang, China
933 (Grant No. E202301005), and the National Natural Science Foundation of China's Research
934 Fund for International Young Scientists (RFIS-I) (Grant No. 42350410442).

935 **References**

- 936 1. Abbas, M., Deparis, J., Isch, A., Mallet, C., Jodry, C., Azaroual, M., Abbar, B., and
937 Baltassat, J.M.: Hydrogeophysical characterization and determination of petrophysical
938 parameters by integrating geophysical and hydrogeological data at the limestone vadose
939 zone of the Beauce aquifer, *Journal of Hydrology*, 615, 128725, 2022.
940 <https://doi.org/10.1016/j.jhydrol.2022.128725>.
- 941 2. Allègre, V., Brodsky, E.E., Xue, L., Nale, S.M., Parker, B.L., and Cherry, J.A.: Using
942 earth-tide induced water pressure changes to measure in situ permeability: A comparison
943 with long-term pumping tests, *Water Resour. Res.*, 52(4), 3113–3126, 2016.
944 <https://doi.org/10.1002/2015WR017346>.
- 945 3. Amiotte Suchet, P., Probst, J.L., and Ludwig, W.: Worldwide distribution of continental
946 rock lithology: Implications for the atmospheric/ soil CO₂ uptake by continental
947 weathering and alkalinity river transport to the oceans, *Glob Biogeochem Cycles*, 17,
948 1038, 2003. <https://doi.org/10.1029/2002GB001891>.
- 949 4. Archie, G.E.: The electrical resistivity log as an aid in determining some reservoir
950 characteristics, *Transactions of the AIME*, 146(1), 54–62, 1942.
951 <https://doi.org/10.2118/942054-G>.

Formatted: Space Before: 1 line, After: 1 line

- 952 5. Asfahani, J.: Estimation of the hydraulic parameters by using an alternative vertical
953 electrical sounding technique: case study from semiarid Khanasser valley region
954 Northern Syria, *Acta Geophys*, 71, 997–1013, 2023. [https://doi.org/10.1007/s11600-022-](https://doi.org/10.1007/s11600-022-00926-0)
955 00926-0.
- 956 6. ASTM.: Standard Test Methods for Measurement of Hydraulic Conductivity of Saturated
957 Porous Materials Using a Flexible Wall Permeameter (ASTM D5084-21), ASTM
958 International, 2021. DOI: 10.1520/D5084-21.
- 959 7. Bauer-Gottwein, P., Gondwe, B.N., Christiansen, L., Herckenrath, D., Kgotlhang, L., and
960 Zimmermann, S.: Hydrogeophysical exploration of three-dimensional salinity anomalies
961 with the time domain electromagnetic method (TDEM), *J. Hydrol.*, 380(3–4), 318–329,
962 2010. <https://doi.org/10.1016/j.jhydrol.2009.11.007>.
- 963 8. Bear, J.: *Dynamics of Fluids in Porous Media*. New York: American Elsevier Publishing
964 Company, 1972.
- 965 9. Binley, A., Cassiani, G., and Deiana, R.: Hydrogeophysics: opportunities and challenges,
966 *Bollettino Di Geofisica Teorica Ed Applicata*, 51(4), 267–287, 2010. [Online]. Available:
967 [http://www.scopus.com/inward/record.url?eid=2-s2.0-](http://www.scopus.com/inward/record.url?eid=2-s2.0-78650438167&partnerID=40&md5=96e14979c82f4b23e8fed0ac0140e7db)
968 78650438167&partnerID=40&md5=96e14979c82f4b23e8fed0ac0140e7db.
- 969 10. Binley, A., Hubbard, S.S., Huisman, J.A., Revil, A., Robinson, D.A., Singha, K., and
970 Slater, L.D.: The emergence of hydrogeophysics for improved understanding of
971 subsurface processes over multiple scales, *Water Resources Research*, 51(6), 3837–3866,
972 2015. <https://doi.org/10.1002/2015WR017016>.

- 973 11. Borah, U.K., and Patro, P.K.: Estimation of the depth of investigation in the
974 magnetotelluric method from the phase, *Geophysics*, 84 (6), E377–E385, 2019.
975 <https://doi.org/10.1190/geo2018-0124.1>.
- 976 12. Brace, W.F., Walsh, J.B., and Frangos, W.T.: Permeability of granite under high pressure,
977 *Journal of Geophysical Research*, 73(6), 2225–2236, 1968.
978 <https://doi.org/10.1029/JB073i006p02225>.
- 979 13. Cagniard, L.: Basic theory of the magneto-telluric method of geophysical
980 prospecting, *Geophysics*, 18 (3), 605–635, 1953. <https://doi.org/10.1190/1.1437915>.
- 981 14. Carbillet, L., Griffiths, L., Heap, M.J., Duwiquet, H., Baud, P., Violay, M.E.S., Reuschlé,
982 T., and Guillou-Frottier, L.: The Influence of Micro- and Macrocracks on the
983 Permeability of Granite, *Rock Mech Rock Eng*, 58, 1361–1378, 2024.
984 <https://doi.org/10.1007/s00603-024-04174-0>.
- 985 15. Chapuis, R.P., and Aubertin, M.: Predicting the Coefficient of Permeability of Soils
986 Using the Kozeny-Carman Equation. *E ´cole Polytech. Montr´al*, 2003, [Online].
987 Available: <http://publications.polymtl.ca/2605/>
- 988 16. Condon, L.E., Markovich, K.H., Kelleher, C.A., McDonnell, J.J., Ferguson, G., and
989 McIntosh, J.C.: Where Is the Bottom of a Watershed? *Water Resources Research*, 56(3),
990 e2019WR026010, 2020. <https://doi.org/10.1029/2019WR026010>.
- 991 17. Daily, W., Ramirez, A., LaBrecque, D., and Nitao, J.: Electrical resistivity tomography of
992 vadose water movement, *Water Resources Research*, 28(5), 1429–1442, 1992.
993 <https://doi.org/10.1029/91WR03087>.

- 994 18. DallaValle, J.M.: Flow of Gases through Porous Media. P. C. Carman, Academic Press,
995 New York; Butterworths, London, 1956. 182 pp. Illus, 1956.
996 <https://www.science.org/doi/10.1126/science.124.3234.1254.b>.
- 997 19. Dell'Oca, A., Guadagnini, A., and Riva, M.: Interpretation of multi-scale permeability
998 data through an information theory perspective, *Hydrol. Earth Syst. Sci.*, 24, 3097–3109,
999 2020. <https://doi.org/10.5194/hess-24-3097-2020>.
- 1000 20. Dewandel, B., Lachassagne, P., Wyns, R., Maréchal, J.C., and Krishnamurthy, N.S.: A
1001 generalized 3-D geological and hydrogeological conceptual model of granite aquifers
1002 controlled by single or multiphase weathering, *Journal of Hydrology*, 330(1–2), 260–284,
1003 2006. <https://doi.org/10.1016/j.jhydrol.2006.03.026>.
- 1004 21. Di, Q., Fu, C., An, Z., Wang, R., Wang, G., Wang, M., Qi, S., and Liang, P.: An
1005 application of CSAMT for detecting weak geological structures near the deeply buried
1006 long tunnel of the Shijiazhuang-Taiyuan passenger railway line in the Taihang Mountains,
1007 *Engineering Geology*, 268, 105517, 2020. <https://doi.org/10.1016/j.enggeo.2020.105517>.
- 1008 22. Esmaeilpour, M., Ghanbarian, B., Sousa, R., Peter, R., and King, P.R.: Estimating
1009 Permeability and Its Scale Dependence at Pore Scale Using Renormalization Group
1010 Theory, *Water Resources Research*, 59 (5), e2022WR033462, 2023.
1011 <https://doi.org/10.1029/2022WR033462>.
- 1012 23. Ferguson, G., McIntosh, J.C., Jasechko, S., Kim, J.H., Famiglietti, J.S., and McDonnell,
1013 J.J.: Groundwater deeper than 500 m contributes less than 0.1% of global river
1014 discharge, *Communication Earth and Environment*, 4, 48, 2023.
1015 <https://doi.org/10.1038/s43247-023-00697-6>.

- 1016 24. Fernando, A., and Pacheco, L.: Regional groundwater flow in hard rocks, *Science of the*
1017 *Total Environment*, 506–507, 182–195, 2015.
1018 <https://doi.org/10.1016/j.scitotenv.2014.11.008>.
- 1019 25. Ferré, T., Bentley, L., Binley, A., Linde, N., Kemna, A., Singha, K., Holliger,
1020 k., Huisman, J.A., Minsley, B.: Critical Steps for the Continuing Advancement of
1021 Hydrogeophysics. *Eos, Transactions American Geophysical Union*, 90(23), 200, 2009.
1022 <https://doi.org/10.1029/2009EO230004>.
- 1023 26. Fiandaca, G., Maurya, P.K., Balbarini, N., Hördt, A., Christiansen, A.V., Foged, N.,
1024 Bjerg, P.L., and Auken, E.: Permeability estimation directly from logging-while-drilling
1025 induced polarization data, *Water Resources Research*, 54, 2851–2870,
1026 2018. <https://doi.org/10.1002/2017WR022411>.
- 1027 27. Fu, C., Di, Q., and An, Z.: Application of the CSAMT method to groundwater
1028 exploration in a metropolitan environment, *Geophysics*, 78 (5), B201–B209, 2013.
1029 <https://doi.org/10.1190/geo2012-0533.1>.
- 1030 28. Fusheng, G., Haiyan, Y., Zengqian, H., Zhichun, W., Ziyu, L., Guocan, W., Linfu, X., Ye,
1031 G., and Wanpeng, Z.: Structural setting of the Zoujiashan-Julong'an region, Xiangshan
1032 volcanic basin, China, interpreted from modern CSAMT data, *Ore Geology Reviews*, 150,
1033 105180, 2022. <https://doi.org/10.1016/j.oregeorev.2022.105180>.
- 1034 29. Gerke, H.H., Dusek, J., and Vogel, T.: Mass transfer effects in 2-D dual-permeability
1035 modeling of field preferential bromide leaching with drain effluent, *Hydrol. Earth Syst.*
1036 *Sci. Discuss.*, 8, 5917–5967, 2011. <https://doi.org/10.5194/hessd-8-5917-2011>.
- 1037 30. Gleeson, T., Moosdorf, N., Hartmann, J., and van Beek, L.P.H.: A glimpse beneath
1038 earth's surface: Global hydrogeology maps (GLHYMPS) of permeability and porosity,

- 1039 Geophysical Research Letters, 41(11), 3891–3898, 2014.
1040 <https://doi.org/10.1002/2014GL059856>.
- 1041 31. Glover, P.W.J.: Geophysical properties of the near surface Earth: electrical properties,
1042 Treatise on Geophysics, 11, 89–137, 2015. [https://doi.org/10.1016/B978-0-444-53802-](https://doi.org/10.1016/B978-0-444-53802-4.00189-5)
1043 [4.00189-5](https://doi.org/10.1016/B978-0-444-53802-4.00189-5).
- 1044 32. Glover, P.W.J.: What is the cementation exponent? A new interpretation, The Leading
1045 Edge, 28(1), 82–85, 2009. <https://doi.org/10.1190/1.3064150>.
- 1046 33. Gonzalez-Duque, D., Gomez-Velez, J.D., Person, M.A., Kelley, S., Key, K., and Lucero,
1047 D.: Groundwater Circulation Within the Mountain Block: Combining Flow and Transport
1048 Models With Magnetotelluric Observations to Untangle Its Nested Nature, Water
1049 Resources Research, 60(4), e2023WR035906, 2024.
1050 <https://doi.org/10.1029/2023WR035906>.
- 1051 34. Hasan, M., and Shang, Y.: Geophysical evaluation of geological model uncertainty for
1052 infrastructure design and groundwater assessments, Engineering Geology, 299, 106560,
1053 2022. <https://doi.org/10.1016/j.enggeo.2022.106560>.
- 1054 35. Hasan, M., Shang, Y., Jin, W., and Akhter, G.: Estimation of hydraulic parameters in a
1055 hard rock aquifer using integrated surface geoelectrical method and pumping test data in
1056 southeast Guangdong China, Geosci J, 25 (2), 223–242, 2021.
1057 <https://doi.org/10.1007/s12303-020-0018-7>.
- 1058 36. Hasan, M., Su, L., Cui, P., and Shang, Y.: Development of deep-underground
1059 engineering structures via 2D and 3D RQD prediction using non-invasive
1060 CSAMT, Scientific Reports, 15, 1403, 2025. <https://doi.org/10.1038/s41598-025-85626-7>.

- 1061 37. Herckenrath, D., Auken, E., Christiansen, L., Behroozmand, A.A., and Bauer - Gottwein,
1062 P.: Coupled hydrogeophysical inversion using time-lapse magnetic resonance sounding
1063 and time-lapse gravity data for hydraulic aquifer testing: Will it work in practice? *Water*
1064 *Resources Research*, 48(1), W01539, 2012. <https://doi.org/10.1029/2011WR010411>.
- 1065 38. Herckenrath, D., Odlum, N., Nenna, V., Knight, R., Auken, E., and Bauer - Gottwein, P.:
1066 Calibrating a Salt Water Intrusion Model with Time-Domain Electromagnetic Data,
1067 *Groundwater*, 51(3), 385–397, 2013. <https://doi.org/10.1111/j.1745-6584.2012.00974.x>.
- 1068 39. Hinnell, A.C., Ferré, T.P.A., Vrugt, J.A., Huisman, J.A., Moysey, S., Rings, J., and
1069 Kowalsky, M.B.: Improved extraction of hydrologic information from geophysical data
1070 through coupled hydrogeophysical inversion, *Water Resources Research*, 46(4), W00D40,
1071 2010. <https://doi.org/10.1029/2008WR007060>.
- 1072 40. Hu, X.Y., Peng, R.H., Wu, G.J., Wang, W.P., Huo, G.P., and Han, B.: Mineral
1073 exploration using CSAMT data: application to Longmen region metallogenic belt,
1074 Guangdong Province, China, *Geophysics*, 78, B111–B119, 2013.
1075 <https://doi.org/10.1190/geo2012-0115.1>.
- 1076 41. Ingebritsen, S.E., and Manning, C.E.: Permeability of the continental crust: dynamic
1077 variations inferred from seismicity and metamorphism, *Geofluids*, 10, 193–205, 2010.
1078 <https://doi.org/10.1111/j.1468-8123.2010.00278.x>.
- 1079 42. ISRM.: Suggested methods for rock characterization, testing and monitoring: 2007–2014,
1080 Springer, 2015. <https://doi.org/10.1007/978-3-319-07713-0>.
- 1081 43. Jardani, A., Revil, A., Santos, F., Fauchard, C., and Dupont, J.P.: Detection of
1082 preferential infiltration pathways in sinkholes using joint inversion of self - potential and

1083 EM - 34 conductivity data, *Geophysical Prospecting*, 55(5), 749–760, 2007.
1084 <https://doi.org/10.1111/j.1365-2478.2007.00638.x>.

1085 44. Jasechko, S., Seybold, H., Perrone, D., Fan, Y., Shamsudduha, M., Taylor, R.G., Fallatah,
1086 O., and Kirchner, J.W.: Rapid groundwater decline and some cases of recovery in
1087 aquifers globally, *Nature*, 625, 715–721, 2024. [https://doi.org/10.1038/s41586-023-](https://doi.org/10.1038/s41586-023-06879-8)
1088 [06879-8](https://doi.org/10.1038/s41586-023-06879-8).

1089 45. Jiang, X.W., Wan, L., Wang, J.Z., Yin, B.X., Fu, W.X., and Lin, C.H.: Field
1090 identification of groundwater flow systems and hydraulic traps in drainage basins using a
1091 geophysical method, *Geophysical Research Letters*, 41(8), 2812–2819, 2014.
1092 <https://doi.org/10.1002/2014GL059579>.

1093 46. Kouadio, K.L., Liu, R., Malory, A.O., and Liu, C.: A novel approach for water reservoir
1094 mapping using controlled source audio-frequency magnetotelluric in Xingning area,
1095 Hunan Province, China, *Geophysical Prospecting*, 71, 1708–1727, 2023.
1096 <https://doi.org/10.1111/1365-2478.13385>.

1097 47. Laghari, A.N., Vanham, D., and Rauch, W.: The Indus basin in the framework of current
1098 and future water resources management, *Hydrology and Earth System Sciences*, 16 (4),
1099 1063–1083, 2012. <https://doi.org/10.5194/hess-16-1063-2012>.

1100 48. Majumdar, R.K., and Das, D.: Hydrological characterization and estimation of aquifer
1101 properties from electrical sounding data in Sagar Island region, South 24 Parganas, West
1102 Bengal, India, *Asian J Earth Sci*, 4, 60–74, 2011.
1103 <http://dx.doi.org/10.3923/ajes.2011.60.74>.

- 1104 49. Manning, C.E., and Ingebritsen, S.E.: Permeability of the continental crust: Implications
1105 of geothermal data and metamorphic systems, *Reviews of Geophysics*, 37(1), 127–150,
1106 1999. <https://doi.org/10.1029/1998RG900002>.
- 1107 50. Mira Geoscience Ltd.: GOCAD Mining Suite 3D Geological Modeling Software. Nancy
1108 University, Lorraine, France, 1999.
- 1109 51. Mudunuru, M.K., Cromwell, E.L.D., Wang, H., and Chen, X.: Deep learning to estimate
1110 permeability using geophysical data, *Advances in Water Resources*, 167, 104272, 2022.
1111 <https://doi.org/10.1016/j.advwatres.2022.104272>.
- 1112 52. Niwas, S., and De Lima, O.A.L.: Aquifer parameter estimation from surface resistivity
1113 data, *Groundwater*, 41, 94–99, 2003. <https://doi.org/10.1111/j.1745-6584.2003.tb02572.x>.
- 1114 53. Nwosu, L.I., Nwankwo, C.N., and Ekine, A.S.: Geoelectric investigation of the hydraulic
1115 properties of the aquiferous zones for evaluation of groundwater potentials in the
1116 complex geological area of imostate, Nigeria, *Asian J Earth Sci*, 6, 1–15, 2013.
1117 <https://scialert.net/abstract/?doi=ajes.2013.1.15>.
- 1118 54. Pellet, H., Arfib, B., Henry, P., Touron, S., and Gassier, G.: Mesoscale permeability
1119 variations estimated from natural airflows in the decorated Cosquer Cave (southeastern
1120 France), *Hydrol. Earth Syst. Sci.*, 28, 4035–4057, 2024. [https://doi.org/10.5194/hess-28-](https://doi.org/10.5194/hess-28-4035-2024)
1121 [4035-2024](https://doi.org/10.5194/hess-28-4035-2024).
- 1122 55. Phoenix Geophysics CMTPro, The Canadian Phoenix CMT Pro Version software for
1123 CSAMT data processing. Toronto, Ontario, Canada, 2020.
- 1124 56. Phoenix Geophysics CSAMT-SW, The Canadian Phoenix CSAMT-SW Version software
1125 for CSAMT data inversion. Toronto, Ontario, Canada, 2020.

- 1126 57. Pollock, D., and Cirpka, O.A.: Fully coupled hydrogeophysical inversion of a laboratory
1127 salt tracer experiment monitored by electrical resistivity tomography, *Water Resources*
1128 *Research*, 48(1), W01505, 2012. <https://doi.org/10.1029/2011WR010779>.
- 1129 58. Qin, X.: Application of Unwedge program to geological stability analysis of deep buried
1130 deposits, *Comprehensive*, 8, 270–273, 2017 (In Chinese).
- 1131 59. Revil, A., and Cathles III, L.M.: Permeability of shaly sands, *Water Resources Research*,
1132 35(3), 651–662, 1999. <https://doi.org/10.1029/98WR02700>.
- 1133 60. Rodi, W., and Mackie, R.L.: Nonlinear conjugate gradients algorithm for 2-D
1134 magnetotelluric inversion, *Geophysics*, 66 (1), 174–187, 2001.
1135 <https://doi.org/10.1190/1.1444893>.
- 1136 61. Saar, M.O., and Manga, M.: Depth dependence of permeability in the Oregon Cascades
1137 inferred from hydrogeologic, thermal, seismic, and magmatic modeling constraints,
1138 *Journal of Geophysical Research*, 109(B4), B04204, 2004.
1139 <https://doi.org/10.1029/2003JB002855>
- 1140 62. Simpson, F., and Bahr, K.: *Practical magnetotellurics*. Cambridge University Press,
1141 Cambridge. 254 pp, 2005. <https://doi.org/10.1017/CBO9780511614095>.
- 1142 63. Singh, K.P.: Nonlinear estimation of aquifer parameters from surficial resistivity
1143 measurements, *Hydrology and Earth System Sciences Discussions*, 2 (3), 917–938, 2005.
1144 <https://doi.org/10.5194/hessd-2-917-2005>.
- 1145 64. Smith, J.T., and Booker, J.R.: Rapid inversion of two- and three-dimensional
1146 magnetotelluric data, *Journal of Geophysical Research: Solid Earth*, 96 (B3), 3905–3922,
1147 1991. <https://doi.org/10.1029/90JB02416>.

- 1148 65. Soupios, P.M., Kouli, M., Vallianatos, F., Vafidis, A., and Stavroulakis, G.: Estimation of
1149 aquifer hydraulic parameters from surficial geophysical methods: a case study of Keritis
1150 Basin in Chania (Crete–Greece), *J Hydrol*, 1, 122–131, 2007.
1151 <https://doi.org/10.1016/j.jhydrol.2007.02.028>.
- 1152 66. Wada, Y., Van Beek, L.P., Van Kempen, C.M., Reckman, J.W., Vasak, S., and Bierkens,
1153 M.F.: Global depletion of groundwater resources, *Geophysical Research Letters*, 37 (20),
1154 L20402, 2010. <https://doi.org/10.1029/2010GL044571>.
- 1155 67. Wang, R., Yin, C., Wang, M., and Di, Q.: Laterally constrained inversion for CSAMT
1156 data interpretation, *Journal of Applied Geophysics*, 121, 63–70, 2015.
1157 <https://doi.org/10.1016/j.jappgeo.2015.07.009>.
- 1158 68. Waxman, M.H., and Smits, L.J.M.: Electrical conductivities in oil-bearing shaly sands,
1159 *Society of Petroleum Engineers Journal*, 8(02), 107–122, 1968.
1160 <https://doi.org/10.2118/1863-A>.
- 1161 69. Webring, M.W.: MINC: A Gridding Program Based on Minimum Curvature: U.S.
1162 Geological Survey Open File Report, 81–1224, p. 41p, 1981.
1163 <https://doi.org/10.3133/ofr811224>.
- 1164 70. Worthington, S.R.H., Davies, G.J., and Alexander, E.C. Jr.: Enhancement of bedrock
1165 permeability by weathering, *Earth-Sci Rev*, 160, 188–202, 2016.
1166 <https://doi.org/10.1016/j.earscirev.2016.07.002>.
- 1167 71. Yan, Y., Ma, L., Qian, J., Zhao, G., Fang, Y., Ma, H., and Wang, J.: Estimating
1168 permeability of rock fracture based on geometrical aperture using geoelectrical
1169 monitoring, *Journal of Hydrology*, 644, 132067, 2024.
1170 <https://doi.org/10.1016/j.jhydrol.2024.132067>.

- 1171 72. Yang, J., Zhang, H., and Cui, Z.: Stability Analysis and Countermeasures of Rock Block
1172 in Underground Cavern, *Guangdong Water Resources and Hydropower* 5, 23–27, 2021
1173 (In Chinese)
- 1174 73. Zhang, M., Farquharson, C.G., and Liu, C.: Improved controlled source audio-frequency
1175 magnetotelluric method apparent resistivity pseudo-sections based on the frequency and
1176 frequency–spatial gradients of electromagnetic fields, *Geophysical Prospecting*, 69, 474–
1177 490, 2021. <https://doi.org/10.1111/1365-2478.13059>.
- 1178 74. Zhu, L., Gong, H., Dai, Z., Guo, G., and Teatini, P.: Modeling 3-D permeability
1179 distribution in alluvial fans using facies architecture and geophysical acquisitions, *Hydrol.*
1180 *Earth Syst. Sci.*, 21, 721–733, 2017. <https://doi.org/10.5194/hess-21-721-2017>.
- 1181 75. Zonge, K.L., and Hughes, L.J.: Kenneth L. Zonge and Larry J. Hughes, (1991), "9.
1182 Controlled Source Audio-Frequency Magnetotellurics," *Investigations in Geophysics*,
1183 713–810, 1991. <https://doi.org/10.1190/1.9781560802686.ch9>.